Parallel organization of cerebellar pathways to sensorimotor, associative, and modulatory forebrain

Thomas J. Pisano[1], Zahra M. Dhanerawala[1], Mikhail Kislin[1], Dariya Bakshinskaya[1], Esteban A. Engel[1], Junuk Lee[1], Nina L. de Oude[2], Kannan Umadevi Venkataraju[3], Jessica L. Verpeut[1], Henk-Jan Boele[1,2], and Samuel S.-H. Wang[1*]

[1]Neuroscience Institute, Washington Road, Princeton University, Princeton, NJ 08544 USA.
[2]Department of Neuroscience, Erasmus MC, 3000 DR Rotterdam, The Netherlands.
[3]Cold Spring Harbor Laboratory, One Bungtown Road, Cold Spring Harbor, NY 11724 USA.

*Corresponding author.

Correspondence: Samuel S.-H. Wang
Neuroscience Institute, Washington Road
Princeton University
Princeton, New Jersey 08544 USA
sswang@princeton.edu
+1 (609) 258-0388

Abstract

Cerebellar outputs take multisynaptic paths to reach higher brain areas, impeding tracing efforts. Here we quantify pathways between cerebellum and contralateral thalamic/corticostriatal structures using the anterograde transsynaptic tracer herpes simplex virus type 1 (H129), the retrograde tracer pseudorabies virus (Bartha), adeno-associated virus, and a whole-brain pipeline for neuron-level analysis using light-sheet microscopy. In ascending pathways, sensorimotor regions contained the most labeled neurons, but higher densities were found in associative areas, including orbital, anterior cingulate, prelimbic, and infralimbic cortex. Ascending paths passed through most thalamic nuclei, especially ventral posteromedial and lateral posterior (sensorimotor), mediodorsal (associative), and reticular (modulatory) nuclei. Retrograde tracing revealed descending paths originating largely from somatomotor cortex. Patterns of ascending influence correlated with anatomical pathway strengths, as measured by brainwide mapping of c-Fos responses to optogenetic inhibition of Purkinje cells. Our results reveal parallel functional networks linking cerebellum to forebrain and suggest that cerebellum uses sensory-motor information to guide both movement and nonmotor functions.

INTRODUCTION

The cerebellum has an increasingly recognized role in nonmotor processing[1–3]. Patients with cerebellar damage show multiple cognitive and affective symptoms[1], and damage at birth leads to autism spectrum disorder (ASD) in half of cases[4–6]. These observations suggest a broad role for the cerebellum in nonmotor function during development and adulthood.

However, the pathways that mediate these influences are poorly characterized. Of particular interest is the cerebellum's partnership with neocortex, especially in cognitive domains[7], as these two structures are the second-largest and largest divisions, respectively, of

41 most mammalian brains[8]. The major descending corticocerebellar pathway passes through the
42 pons and the majority of returning ascending fibers pass through the thalamus[9,10], comprising
43 two massive within-brain long-distance pathways[11]. Other polysynaptic pathways exist between
44 the cerebellum and neocortex, including a smaller ascending pathway through ventral tegmental
45 area that has attracted recent interest[12]. These descending and ascending pathways are
46 suggested to form closed loops[13], giving each cerebellar region one or more specific neocortical
47 partners with which it exchanges information.

48 This picture lacks critical information: the identity of those distant regions, which have
49 been difficult to map. Given the brain-wide nature of cerebello-cortical pathways, researchers
50 have used large-scale approaches to examine the functional significance of these pathways.
51 Transcranial magnetic stimulation in humans demonstrated that the cerebellum influences
52 neocortical excitability[14], including cognitive and affective circuits[15]. Functional MRI can attain
53 subcentimeter resolution, detect long-distance correlations[16], and when coupled with cerebellar
54 stimulation, demonstrate causal relationships[17]. Functional imaging at cellular resolution in
55 nonhuman animals has been made possible by visualizing c-Fos, an immediate-early gene
56 product whose expression is regulated by neural activity. Although useful in demonstrating
57 communication with distant brain regions, these methods do not provide cellular-resolution
58 information about cerebello-cortical circuits.

59 Pathways entering and exiting the cerebellum pass through synapses in the brainstem
60 and the cerebellum itself, blocking the passage of most cellular tracer molecules. However, this
61 problem can be overcome using transsynaptically transported viruses[18]. The H129 strain of
62 herpes simplex virus type 1 (HSV-H129) is a reliable, largely anterograde tracer that can identify
63 long-distance targets of specific brain regions. For retrograde tracing, the Bartha strain of
64 pseudorabies virus (PRV-Bartha) allows efficient, synapse-specific transport. Thus recent
65 molecular technology opens a means of mapping the cerebellum to its brainwide information-
66 processing partners.

67 A circuit-level understanding of cerebello-cortical connectivity is needed to better probe
68 how abnormalities can lead to neurocognitive disorders like ASD. Viral tracing and cellular
69 activity measurements enable cellular-level dissection of cerebello-cortical pathways, but
70 conventional histological methods are too laborious for quantifying connectivity in the whole
71 brain at once. But with the recent advent of optimized tissue clearing techniques with light-sheet
72 microscopy[19], the same tracing methods can now be scaled to cover entire brains. The resulting
73 imaging datasets can occupy terabytes, creating a need for computationally efficient cell
74 detection and anatomical assignment. These challenges can be addressed using machine
75 learning algorithms to detect neurons and image registration methods to align brains. For the
76 cerebellum, an additional problem is the absence of a reference template: the current field
77 standard, the Allen Brain Atlas, omits the posterior two-thirds of the cerebellum. Any integrative
78 study of cerebellar anatomy and function must therefore start with the creation of a suitable
79 atlas.
80 In this project, we used HSV-H129 to map the cerebellum's direct ascending outputs to
81 the thalamus and striatum and disynaptic paths to the neocortex, and PRV-Bartha to map
82 descending paths from neocortex to cerebellum. We then used these measurements to
83 generate a brainwide atlas of cerebellum-forebrain connectivity. We developed an analysis
84 pipeline that allows per-region cell counts to be converted from cell counts to per-volume cell
85 density, giving a measure of relative impact on local circuitry. The impact of ascending paths
86 was confirmed using optogenetic stimulation of c-Fos expression. All measurements were
87 referred to a whole-brain atlas that includes the entire cerebellum. Taken together, our results
88 provide a brainwide map of the cerebellum's paths to and from thalamo-cortical-striatal systems,
89 providing insight into possible cerebellar contributions to whole-brain function and
90 neurocognitive disorders.

91 **RESULTS**

92 **Transsynaptic viral labeling reveals distant cerebellar targets**

93 To trace transsynaptic pathways from cerebellum to midbrain and neocortex, we used
94 HSV-H129-VC22 (**Figure 1a**), an HSV-H129 recombinant virus that expresses enhanced green
95 fluorescent protein (EGFP) targeted by means of a localization sequence to the cell nucleus.
96 Transsynaptic viral tracing yields weaker labeling of cells compared with longer-expression-time
97 strategies such as AAV-driven fluorophore expression. To achieve high signal-to-noise ratio, we
98 used iDISCO+, a method that combines tissue clearing with whole-brain immunostaining using
99 Dako anti-HSV antibody with light-sheet microscopy.

100 To determine the optimal timepoints for examining disynaptic (i.e. Purkinje cell to deep
101 nuclear to thalamic) and trisynaptic (Purkinje cell to deep nuclear to thalamic to neocortical)
102 targets, we injected H129-VC22 into the cerebellar cortex of mice and examined tissue between
103 30 and 89 hours post-injection (hpi; **Figure 1b,c**). At 54 hpi, labeling was observed in thalamus
104 with little visible neocortical labeling (**Figure 1c,d**), so we defined 54 hpi as the thalamic
105 timepoint. Labeling was also seen in other midbrain and hindbrain areas, consistent with known
106 monosynaptic targets of the cerebellar nuclei[20]. Neocortical labeling was visible first at 73 hours
107 and throughout neocortex at 82 hpi. These timepoints are consistent with prior studies using
108 conventional histological methods[2,12].

109 **Automated cell detection using a convolutional neural network**

110 Each brain generated a dataset exceeding 100 gigabytes. To automate cell detection,
111 we trained a three-dimensional convolutional neural network (CNN) to recognize neurons. A
112 CNN with U-Net architecture running on a GPU-based cluster was trained by supervised
113 learning using more than 3600 human-annotated centers of cells as ground truth (**Figure 1e**;
114 **Table 1**). The performance at different likelihood thresholds was plotted as a receiver-operator

115 curve of precision and recall (**Figure 1f**), where precision was defined as the number of true
116 positives divided by all positives, and recall was defined as the number of true positives divided
117 by the number of true positives plus false negatives. A threshold likelihood of 0.6 was found to
118 maximize the harmonic mean of precision and recall, a quantity known as the F1 score.
119 Querying the CNN with the testing dataset gave an F1 score of 0.864, nearly the F1 score for
120 human-human concordance, 0.891, indicating that the CNN had successfully generalized to
121 whole-brain datasets.

122 **Generation of the Princeton Mouse Atlas**

123 To overcome past difficulties in registering images taken using different modalities, we
124 devised a two-step procedure to calculate an averaged light-sheet-based brain template for
125 referral to the Allen Brain Atlas (**Figure 2**). After this procedure, individual light-sheet brains
126 were fitted to this template. The Allen Brain volumetric Atlas (ABA), a field standard, is based on
127 serial two-photon microscopy and lacks a complete cerebellum (**Figure 2a**). To remedy that lack
128 and to generate a template useful for our light-sheet images, we constructed a Princeton Mouse
129 brain Atlas (PMA; **Supplementary Figure 1**). To make the PMA compatible with Allen
130 standards, we computed a transform to convert it to Allen Brain CCFv3 space (**Figure 2b**). We
131 then extended the space using manually-drawn contours to generate a complete, annotated
132 cerebellar anatomy (**Figure 2c,d**) that included posterior lobules (**Figure 2c,d** red lines;
133 **Supplementary Figure 2**).
134 To quantify the precision of atlas registration, we asked blinded users to find readily
135 identifiable points in our atlas and in four sets of unregistered, affine-only registered, and fully
136 registered volumes (**Figure 2b**; **Supplementary Figure 3**). After registration, the median
137 Euclidean distance from complementary points in the PMA was 93 ± 36 μm (median ±
138 estimated standard deviation) to b-spline registered volumes. Blinded users determined points

139 in the same volume twice to establish an intrinsic minimum limit of 49 ± 40 μm. Assuming that
140 uncertainties sum as independent variables, the estimated accuracy of the registration method
141 was $\sqrt{(93^2-49^2)}$ = 79 μm, or 4 voxels.

142 **Cerebellar paths to ventral tegmental area are weaker than thalamic projections**

143 Among other monosynaptic targets of the cerebellar nuclei, an area of renewed focus
144 has been the ventral tegmental area (VTA)[26,27], including a recent report of cerebellar influence
145 over reward processing[12]. We used our anterograde tracing pipeline to compare the relative
146 projection strengths of contralateral cerebellar paths to thalamus and two midbrain
147 dopaminergic areas, VTA and the substantia nigra (**Supplementary Figure 4**). We found that
148 the total number of neurons in contralateral VTA[28] was considerably lower than in thalamic
149 regions, consistent with known tracing[12,20,21,27]. Normalized to density per unit volume of the
150 target region, VTA projections were less than one-third as strong as projections to VPM, MD,
151 and RTN. Neuron densities in substantia nigra (SNr and SNc) were mostly lower than in VTA. In
152 summary, cerebellar projections to VTA constituted a moderate-strength projection, smaller in
153 strength than thalamic pathways but greater than other dopaminergic targets.
154 Like the VTA, striatal regions are also involved in reward learning. The cerebellar cortex
155 is known to project to basal ganglia trisynaptically via the cerebellar nuclei and thalamus[29].
156 Among striatal regions, at our neocortical labeling timepoint, we observed the most labeling in
157 the caudate followed by the nucleus accumbens and the central amygdala (**Supplementary**
158 **Figure 5**). Dense clusters of labeled cells were found in the dorsal striatum (**Supplementary**
159 **Figure 6**), suggestive of striosomes, which convey reward prediction or error information[30]. At
160 the neocortical timepoint we also quantified hypothalamic expression, observing high variability
161 in projection density, likely related to the small volumes of hypothalamic nuclei (**Supplementary**

162 **Figure 7**). We observed the most and densest labeling in the lateral hypothalamic area which
163 has been shown to regulate feeding and reward[31].

164 **The cerebellum sends output to a wide range of thalamic targets**

165 We used our automated analysis pipeline, which we named BrainPipe, to quantify
166 cerebello-thalamic connectivity (**Figure 3a**). We injected 23 brains with H129-VC22 at different
167 sites in the posterior cerebellum (**Figure 3b**) and collected brains at 54 hpi, the thalamic
168 timepoint. At this time, the number of neurons per region were widely distributed among
169 contralateral thalamic regions (**Figure 3c**). The density of neurons observed in neocortical
170 regions was 0.085 ± 0.073 (mean ± standard deviation, 17 regions) times that seen in 80 hpi
171 injections, indicating that sufficient time had elapsed to allow transport to thalamus but not
172 neocortex. Number of neurons by region (**Figure 3d**) were not systematically related to
173 anteroposterior position (rank correlation with anteroposterior position r=+0.05), suggesting that
174 the efficiency of labeling was not strongly dependent on differences in transport distance. For
175 display, the number of neurons for each region were converted to percentage of total per-brain
176 thalamic neurons and coded according to “sensory/motor” and “polymodal association”
177 functionalities based on ABA ontology (**Figure 3,** yellow/green shading).

178 The cerebellothalamic tract originates entirely from the deep cerebellar nuclei and
179 ascends through the superior cerebellar peduncle (also known as brachium conjunctivum), with
180 most axons crossing the midline before reaching the thalamus. Consistent with findings that a
181 principal target of cerebellothalamic axons is the ventral thalamus[20,21] a site of somatosensory
182 relay nuclei[22], we found the highest contralateral cell count in the ventral posteromedial nucleus
183 (VPM; **Figure 3c,d,e**), which conveys sensory information from the face and mouth. Other
184 structures with large number of neurons included the nearby ventromedial (VM) and ventral

185 posterolateral (VPL) nuclei. These findings confirm that cerebellar-injected H129-VC22 labels
186 major known pathways to thalamus.

187 Prominent labeling was also observed outside the ventral thalamus. After VPM, the
188 contralateral structure with the second-largest fraction of expressing cells was the reticular
189 thalamic nucleus (RTN), followed by the lateral posterior (LP) and mediodorsal (MD) nuclei. MD
190 and LP are association thalamic nuclei. MD is engaged in reversal learning[23], sends its output to
191 frontal regions, including insular, orbital, and prelimbic cortex[24], and is engaged in cognitive and
192 working memory tasks in humans[23]. Lobule VI, a site of structural abnormality in ASD[25], had
193 dense projections to MD (**Figure 3f,g**). These results suggest a strong role for cerebellum in
194 flexible cognition. LP sends its output to primary somatosensory cortex, primary and secondary
195 motor cortex, and frontal association area[24]. RTN, unlike other thalamic nuclei, does not project
196 to neocortex, instead sending inhibitory projections to other thalamic nuclei. Thus, major paths
197 from cerebellum to thalamus include both relay nuclei and the other two major classes of nuclei,
198 association (MD, LP) and local modulatory (RTN).

199 To identify specific topographical relationships, we fitted a generalized linear model
200 (GLM; **Figure 3f**), using the fraction-by-lobule of the total cerebellar injection as input
201 parameters, and the fraction-by-nucleus of total thalamic expression as output measurements.
202 The GLM revealed a broad mapping of lobules I-X to a variety of thalamic targets, and a more
203 focused pattern of mapping from simplex, crus I and II, paramedian lobule, and copula
204 pyramidis to specific thalamic targets. Hotspots of mapping included lobules I-X to VPM, RTN,
205 MD, lateral dorsal (LD), VM, VPL, reuniens, anteroventral, and medial habenula; simplex to
206 posterior complex, ventral anterolateral (VA-L), and central medial; crus I to VPM, LP, and
207 anteroventral; crus II to VPM, MD, posterior complex, LD, and VPL; and paramedian lobule and
208 copula pyramidis to LP, parafascicular, ventral lateral geniculate, and central lateral (**Table 2**).

209 **Deep-nuclear direct projections to thalamus are consistent with transsynaptic tracing**

210 As a second approach to characterizing cerebellar projections to thalamus, we injected adeno-
211 associated virus containing the GFP sequence into cerebellar nuclei and characterized the
212 spatial distribution of fluorescent nerve terminals (**Figure 4**). Injections (n=4) of 125 nl (titer
213 7×10^{12} vg/mL) primarily targeted bilateral dentate nuclei and also reached interposed and
214 fastigial nuclei (**Figure 4a**). Three weeks after injection, animals were sacrificed and brains
215 sectioned and imaged by confocal microscopy (**Figure 4b**).

216 Terminals were clearly visible throughout thalamic sites, largely contralateral to the site
217 of injection. Manual counts of varicosities in twenty randomly picked 50 by 50 μm regions were
218 strongly correlated with average brightness ($r = 0.88$, $t = 8.115$, $p < .0001$). Therefore we used
219 summed brightness as a measure of total innervation. Summed brightness was defined as the
220 total fluorescence within a nucleus, summed across all sections where the nucleus was present.
221 Overall, the highest summed brightness was found in ventral thalamic nuclei including VM, VA-
222 L, VPM, and VPL, consistent with previous literature reports and with the density of cells
223 observed in HSV-H129 injections. The nucleus-by-nucleus fluorescence density (i.e. summed
224 brightness divided by the total area covered by the nucleus in the analyzed images) was highly
225 correlated with the HSV-H129 neuron density (**Figure 4c**; Kendall's rank correlation 0.49, $p =$
226 0.01). Taken together, these measurements indicate that HSV-H129 injections at the thalamic
227 timepoint accurately capture the overall pattern of projection from deep nuclei to contralateral
228 thalamus.

229 **Cerebellar paths to neocortex are strongest in somatomotor regions and densest in**
230 **frontal regions**

231 To characterize cerebellar paths to neocortex, we examined 33 HSV-injected brains at
232 80 hpi (**Figure 5a,b,c**). As expected, the majority of neurons were found in contralateral

233 somatosensory and somatomotor areas, with additional neurons found at more anterior and
234 posterior locations (**Figure 5d,f**).

235 When converted to density, a different pattern of projection density became apparent
236 (**Figure 5e,g**). The highest densities of neurons were found in contralateral anterior and medial
237 neocortical regions, with peak regions exceeding 400 neurons per mm^3, more than twice the
238 highest density found in somatosensory and somatomotor regions. The most densely labeled
239 regions included infralimbic, orbital, and prelimbic areas but excluded the frontal pole (**Figure**
240 **5e,g**).

241 We fitted a GLM to the data in the same way as for thalamic labeling. Sensorimotor and
242 frontal regions were strongly represented in the model weights. The GLM also sharpened the
243 cerebellocortical topographical relationship (**Figure 5f**). All injected cerebellar sites showed high
244 weighting in somatomotor and somatosensory cortex. In addition, lobules I-V showed significant
245 weights in anterior cingulate cortex. Weak clusters of connectivity were also visible in visual and
246 retrosplenial cortex. Averaging neuron density by primary injection site (**Figure 5g**) revealed
247 that all injected cerebellar sites sent dense projections to infralimbic cortex. Lobules I-X and
248 crus I and II sent denser projections to infralimbic, prelimbic, and orbital cortex compared to
249 other cerebellar injection sites (**Figure 5g**).

250 **Cerebellum-neocortical paths strongly innervate deep neocortical layer neurons**

251 To investigate the layer-specific contributions of cerebellar paths to neocortex, we
252 examined laminar patterns of expression at the neocortical time point of H129-VC22 injections
253 (**Figure 6**). To minimize near-surface false positives, 60 μm was eroded from layer 1. In most
254 neocortical areas, the most and densest anterogradely labeled neurons were found in layers 5,
255 layers 6a and 6b (**Figure 6b,c**). No differences were found among the layer-specific patterns

256 resulting from injections to anterior vermis, posterior vermis, and posterior hemisphere ($p>0.95$,
257 ANOVA, two-tailed, 3 injection groups).

258 The layer-specificity of thalamocortical connections varies by neocortical region[33,34]. A
259 common motif of thalamocortical projections is strong innervation of layer 6 neurons, especially
260 in sensory regions[35,36]. In sensorimotor regions (somatomotor and somatosensory), over 40% of
261 our labeled cells were found in layer 6, a higher fraction than in other categories of neocortex
262 (**Figure 6b**). However, even though sensory regions are known to receive thalamic innervation
263 of layer 4 neurons[35], labeled layer 4 neurons comprised only 10% of cells in somatosensory
264 cortex and even less in other sensory regions (gustatory, visceral, temporal, visual). Thus
265 cerebellar paths to neocortex emphasized deep-layer neurons and tended to exclude classical
266 layer-4 targets, even in sensorimotor regions.

267 A different pattern was seen in rhinal cortex, which forms part of the medial temporal
268 system for declarative memory. Rhinal regions (perirhinal, ectorhinal, and entorhinal) had the
269 highest fraction of layer 2/3 neurons (**Figure 6b**). This finding recalls the observation that in
270 associative neocortical regions, thalamocortical axons send substantial projections to superficial
271 layers[36]. Frontal and other association regions showed patterns that were intermediate between
272 sensorimotor and rhinal regions, while infralimbic, prelimbic, orbital, and anterior cingulate
273 cortex also received more and denser projections to layer 1 (**Figure 6b**). Taken together, our
274 analysis indicates that cerebellar influences on neocortex arrive first through superficial and
275 deep layer pathways (**Figure 6d**).

276 **Pseudorabies virus reveals strong descending somatomotor influence**

277 To characterize descending paths from neocortex to the cerebellum, we performed a
278 series of injections of pseudorabies virus Bartha strain (PRV-Bartha), a strain that travels
279 entirely in the retrograde direction (**Figure 7a,b,c**). In pilot experiments, expression was strong

280 in neocortex at 80 hpi. To isolate layer 5 neurons, whose axons comprise the descending
281 corticopontine pathway, we analyzed neurons registered to deep layers, which comprised 64%
282 of all contralaterally labeled neocortical neurons.

283 Similar to the anterograde tracing results, the largest proportion of neurons was found in
284 somatosensory and somatomotor areas (**Figure 7d,f**). Normalized to volume, neuron densities
285 were highest in somatosensory, somatomotor, and frontal cortex (**Figure 7e,g**). Two regions
286 identified as sources of corticopontine axons by classical tracing[37] were labeled: anterior
287 cingulate areas from injection of lobule VI and VII, and agranular insular cortex from crus II. In
288 addition, retrosplenial and auditory areas were labeled from injection of paramedian lobule and
289 copula pyramidis.

290 A GLM fitted to the data by the same procedure as the HSV-H129 tracing showed
291 highest weighting in somatomotor, somatosensory, and frontal regions (**Figure 7f**). Weights in
292 retrosplenial and visual cortex were smaller for vermal injections, and weights in gustatory,
293 agranular insula, and visceral cortex were elevated for simplex and crus II injections. Averaging
294 neuron density by primary injection site revealed all injected cerebellar sites received dense
295 projections from somatomotor and somatosensory cortex. Lobules I-VII and crus II received
296 denser projections from anterior cingulate and prelimbic cortex compared to other cerebellar
297 injection sites. Crus II also received dense projections from infralimbic, agranular insula,
298 gustatory, ectorhinal, and visceral cortex.

299 Descending corticopontine projections are known to be largely contralateral. To test the
300 extent to which descending paths remain contralateral across multiple synaptic steps, we
301 quantified the ratio of contralateral to ipsilateral cells for PRV-Bartha injections. Contralateral
302 cells outnumbered ipsilateral cells in all major neocortical areas, with average contralateral-to-
303 ipsilateral ratios of 1.4 in frontal cortex, 1.7 in posterior cortex, and 3.2 in somatomotor and
304 somatosensory cortex. Contralateral-to-ipsilateral ratios were higher for hemispheric injection
305 sites than vermal sites (**Supplementary Table 1**).

306 Ascending axonal projections of cerebellar nuclei are known to largely decussate to
307 reach contralateral midbrain structures[38]. For H129-VC22 injections, we observed bilaterality at
308 both the thalamic and neocortical timepoints. At the thalamic timepoint, the mean ratio of
309 contralateral cells to ipsilateral cells was 2.5 in sensorimotor nuclei and 1.0 in polymodal
310 association nuclei. Contralateral-to-ipsilateral ratios were highest for hemispheric injection sites
311 (**Supplementary Table 1**). Taken together, our HSV-H129 and PRV-Bartha observations
312 suggest that the organization of projections between cerebellum and neocortex is most strongly
313 contralateral in pathways that concern movement, and more symmetrically distributed for
314 nonmotor paths.

315 **c-Fos mapping reveals brainwide patterns of activation consistent with transsynaptic**
316 **tracing**

317 The reciprocal paths we have identified suggest that cerebellum incorporates
318 descending information and influences forebrain processing through diverse thalamocortical
319 paths. To test whether the functional strength of ascending paths was commensurate with their
320 anatomical connection, we measured expression of the immediate early gene c-Fos after
321 optogenetic perturbation of cerebellar activity (**Figure 8**). c-Fos expression reflects cumulative
322 neural activity and provides an independent means of quantifying long-distance influence. We
323 expressed the hyperpolarizing proton pump ArchT in Purkinje cells by injecting rAAV1-CAG-
324 FLEX-ArchT-GFP into the cerebellar vermis of L7-Cre+/- mice, using L7-Cre-/- mice as controls
325 (**Figure 8a**). Inactivation of Purkinje cells, which inhibit neurons of the deep cerebellar nuclei,
326 would be expected to have a net excitatory effect on thalamic and therefore neocortical activity.
327 After 1 hour photostimulation over lobule VI, either in mice expressing ArchT (Cre+/-) or
328 in nonexpressing controls (Cre-/-), brains were removed and cleared using iDISCO+, then
329 immunohistochemically stained for c-Fos using AlexaFluor-790 as the fluorophore, and

330 analyzed using ClearMap (**Figure 8b,c**; **Supplementary Figure 8**) for comparison with HSV-
331 H129 tracing (**Figure 8d**).
332 Fourteen structures were identified having both significant count differences by a
333 nonparametric t-test and an activation ratio (defined as stimulation-group c-Fos average count
334 divided by control-group average) greater than 2.5 (**Figure 8e,f**). The strongest activation ratios
335 occurred in the anterior cingulate cortex, centrolateral nucleus of the thalamus, and the nucleus
336 accumbens (**Figure 8f**). Lobule VI itself also showed elevated c-Fos counts, as expected for
337 pulsed-light inactivation of Purkinje cells[32]. A voxel-wise t-test on cell count volumes
338 (**Supplementary Figure 9**) showed strong c-Fos expression in frontal neocortical regions,
339 especially in deep and middle neocortical layers. In a separate experiment, midline lobule VIa
340 injection of H129-VC22 into Thy1-YFP mice, which express YFP primarily in layer V, revealed
341 viral labeling in frontal cortex subjacent to YFP, coincident with the layer-specificity of c-Fos
342 expression in the optogenetic experiments.
343 Among neocortical regions, the rank order of c-Fos stimulation-to-control cell density
344 differences and H129-VC22 expression density was highly correlated (**Figure 8g**; Kendall's
345 τ=+0.47), indicating that brainwide patterns of neural activity coincide with patterns of ascending
346 polysynaptic targets from lobule VI. Subcortical examination of c-Fos brains revealed further
347 broad similarities in expression with H129-VC22 labeling, including pontine nuclei, midbrain,
348 superior colliculi, and hypothalamus (**Supplementary Figure 10; Supplementary Figure 11**).
349 Overall, these data show that c-Fos-based measures of brain activation coincide well with
350 patterns of anatomical projection as measured by transsynaptic viral labeling.

351 **DISCUSSION**

352 We found that ascending synaptic paths from the cerebellum can be classified into three
353 parallel ascending systems serving sensorimotor, flexible cognitive, and modulatory functions
354 (**Figure 9**). Well-known sensorimotor regions contained the most connections, but nonmotor
355 paths achieved comparable or higher local peak connection densities. Overall, these paths
356 reached nearly all parts of neocortex through a variety of thalamic, striatal, and midbrain
357 structures.

358 In both neocortex and thalamus, the majority of neurons labeled by anterograde (HSV-
359 H129) or retrograde (PRV-Bartha) viruses were found in structures classified as sensorimotor,
360 including ventral anterior (VA), ventrolateral (VL) and ventromedial (VM) thalamic nuclei[39]. By
361 per-volume density, the strongest ascending projections went to anterior cingulate, prelimbic
362 and infralimbic cortex, as well as agranular and orbital areas. In the thalamus, the three thalamic
363 nuclei with the most neurons were VPM (sensorimotor), reticular thalamic (modulatory), and
364 mediodorsal (associative), providing a substrate for a wide variety of brain functions.
365 Descending pathways from neocortex were most strongly concentrated in somatomotor and
366 somatosensory cortex. Taken together, these anatomical tracing patterns suggest that sensory-
367 motor information is used by cerebellum to exert influence on a wide range of motor and
368 nonmotor neocortical functions.

369 **Nonmotor functions of the cerebellum.** Among the cerebellar injection sites, nonmotor
370 functions have been suggested for lobule VI in the posterior vermis, and crus I and II in the
371 posterior parts of the hemispheres. We found that Lobule VI sent strong projections to
372 mediodorsal nucleus of thalamus and to frontal neocortical regions, which serve a wide range of
373 cognitive and emotional functions. Because the refinement of neural circuitry is activity-
374 dependent[40], this projection may also potentially account for the observation that cerebellar
375 perturbation of lobule VI can affect cognitive and social development in rodents[2] and humans[6],

376 and the association of posterior vermal abnormalities to a high risk of ASD[25]. Optogenetic
377 stimulation of lobule VI also led to strong activation of c-Fos in the nucleus accumbens (NAc),
378 the main component of the ventral striatum, which is implicated in reward learning and
379 motivation[41]. This observation is consistent with our observation of NAc labeling at the
380 neocortical timepoint of HSV anterograde tracing.

381 We found that crus I projects to lateral dorsal thalamus and frontal neocortical regions.
382 Crus I has previously been observed to be activated during working memory[43]. In mice,
383 disruptions of crus I activity in adulthood or juvenile life lead to deficits in adult flexible
384 behavior[2,44]; adult disruption shortens the time constant of a working memory task[3]. Crus II
385 projects to a wide variety of sensorimotor (ventral) and non-ventral thalamic nuclei. This may
386 provide a substrate for the observation that juvenile disruption of crus II leads to long-lasting
387 deficits in social preference[2].

388 Midline lobules (I-X) and crus II projected strongly to reticular thalamic nucleus (RTN), a
389 known monosynaptic target of the deep nuclei[45,46]. RTN is of functional interest because it is the
390 only thalamic nucleus that is inhibitory and because it sends projections exclusively within the
391 thalamus itself. RTN may control sensory gain[47] and the flow of information in and out of the
392 neocortex[48]. RTN also receives a strong descending projection from neocortical layer 6[48,49], a
393 site of prominent expression in our work. This descending projection completes an inhibitory
394 loop, and has been suggested to contribute to neocortical oscillations and synchrony[50,51]. Our
395 findings add cerebellum as a substantial contributor to this modulatory thalamocortical network.

396 **A pipeline for long-distance transsynaptic mapping.** Although many individual
397 projections within these pathways have been previously reported, our work presents a brainwide
398 survey of their relative strength. Polysynaptic transsynaptic tracing studies have relied on time-
399 consuming human identification for analysis. Tissue clearing has been used for volumetric
400 histological analyses, with the recent introduction of automated methods for cell identification[19].
401 We find that cell counting can be efficient, accurate, and scalable to the whole brain. Our

402 mapping project relied on our BrainPipe pipeline, which combines transsynaptic tracing, whole-
403 brain clearing and microscopy, automated neuron counting, and atlas registration. BrainPipe
404 should be scalable for larger datasets as the resolution of light-sheet microscopy improves.
405 Adapting BrainPipe to other experimental studies requires only a different annotated dataset to
406 train a new convolutional neural network to identify objects of interest. Our pipeline can run on
407 high-performance computing clusters, allowing for faster turnaround of results than other
408 analysis pipelines, such as ClearMap[19].

409 Our viral transsynaptic approach was designed to identify disynaptic paths from
410 cerebellum to thalamus and trisynaptic paths to neocortex. However, alternative paths are
411 possible. The fastigial nuclei have bilateral efferents to the ipsilateral brachium conjunctivum
412 (BC) and, via the uncinate fasciculus to the contralateral BC[11,52] and the cerebellar nuclei project
413 to hindbrain/midbrain targets in addition to thalamus[11,53]. Indeed, we observed contralateral
414 crossing of axons after AAV injections in the fastigial nucleus (**Supplementary Figure 12**). Over
415 long distances, where transport time is increasingly dominated by axon-associated transport
416 mechanisms[54], HSV-H129 may follow such alternative paths, as well as retrograde paths for
417 incubations of 96 hours or longer. We therefore minimized incubation periods and restricted our
418 analysis to contralateral projections. The correlation of the resulting observed labeling with c-
419 Fos activation suggests that our observations reflect major routes by which the cerebellum
420 influences neocortical function.

421 In creating our light-sheet brain atlas, we overcame the general problem of creating a
422 reference atlas for a different imaging modality from the ABA. Our solution consisted of three
423 steps: (1) align individually imaged brains to a single experimental brain serving as the initial
424 template, (2) average the post-aligned brains to obtain a project-specific atlas for precise
425 automated registration, and (3) learn the transform between the project-specific atlas and the
426 field standard. Our basic software package (github.com/PrincetonUniversity/pytlas) is capable of
427 efficiently generating atlases for other imaging modalities as well.

428 **From local cerebellar circuitry to global brain function.** The local circuitry of
429 cerebellum is thought to make rapid predictions about future states, which then modulate the
430 activity of other brain regions. In the motor domain, evidence suggests error learning through a
431 supervised learning process. Contextual information in this learning process comes from the
432 mossy fiber-granule cell pathway, and a teaching signal comes from the climbing fiber pathway.
433 This circuitry is homologous across cerebellar regions, with each part of the cerebellar cortex
434 managing a massive convergence of diverse incoming information from a distinct assortment of
435 distant brain regions. Purkinje cells integrate this convergence to generate subsecond
436 predictions converging on cerebellar and vestibular nuclei, which serve as an exit gateway for
437 influencing target brain regions[11]. The cerebellum may generate predictions to fine-tune activity
438 across nonmotor functions as well[3,6,55] as it is composed of many modules, each with its own
439 specific extracerebellar partners[56].

440 In this work, we mapped the efferent paths that convey cerebellar ascending output to
441 show that nearly every neocortical region is potentially influenced by cerebellar processing. To
442 complete the picture, it will be necessary to perform similar mapping of inputs to the cerebellum.
443 Increasingly sophisticated genetic and viral methods make it possible to trace polysynaptic input
444 streams separately through the pons and the inferior olive[11]. It is also possible to perturb and
445 monitor both input and output pathways with high precision. Such approaches will reveal the
446 many contributions of cerebellum to global brain function.

447 **METHODS**

448 **OVERVIEW OF AUTOMATED PIPELINE FOR TRANSSYNAPTIC TRACING**

449 In order to identify and quantify cerebellar connectivity on the long distance scale, we developed
450 a pipeline, BrainPipe, to enable automated detection of transsynaptically labeled neurons using
451 the mostly anterogradely-transported HSV-H129[57], identifying cerebellar output targets, and
452 retrogradely-transported PRV-Bartha[58], identifying the descending corticopontine pathway,
453 comprised mostly of layer V pyramidal neurons[59]. Mouse brains with cerebellar cortical
454 injections of Bartha or H129 were cleared using iDISCO+. We then imaged the brains using
455 light-sheet microscopy, generating brain volumes with a custom Python package. Next, to
456 ensure accurate anatomical identification across brains, we created a local light-sheet template,
457 the Princeton Mouse Brain Atlas (PMA) and quantified registration performance of individual
458 volumes to the local template. We then determined the transform between the PMA and the
459 Allen Brain Atlas, enabling standardization of our results with the current field standard. Next, to
460 automatically and accurately detect labeled cells, we developed a convolutional neural network
461 whose performance approached that of human classifiers.

462 **ANIMAL EXPERIMENTATION**

463 Experimental procedures were approved by the Princeton University Institutional Animal Care
464 and Use Committee (protocol number 1943-19) and performed in accordance with the animal
465 welfare guidelines of the National Institutes of Health.

466 **VIRUS SOURCES**

467 HSV-1 strain H129 recombinant VC22 (H129-VC22) expresses EGFP-NLS, driven by the CMV
468 immediate-early promoter and terminated with the SV40 polyA sequence. To engineer this
469 recombinant, we used the procedure previously described to construct HSV-772, which

470 corresponds to H129 with CMV-EGFP-SV40pA[57]. We generated plasmid VC22 by inserting into
471 plasmid HSV-772 three tandem copies of the sequence for the c-Myc nuclear localization signal
472 (NLS) PAAKRVKLD[60], fused to the carboxy-terminus of EGFP. Plasmid VC22 contains two
473 flanking sequences, one of 1888-bp homologous to HSV-1 UL26/26.5, and one of 2078-bp
474 homologous to HSV-1 UL27, to allow insertion in the region between these genes. HSV-1 H129
475 nucleocapsid DNA was cotransfected with linearized plasmid VC22 using Lipofectamine 2000
476 over African green monkey kidney epithelial cell line Vero (ATCC cell line CCL-81), following the
477 manufacturer's protocol (Invitrogen). Viral plaques expressing EGFP-NLS were visualized and
478 selected under an epifluorescence microscope. PRV-152 (PRV Bartha[58]), which drives the
479 expression of GFP driven by the CMV immediate-early promoter and terminated with the SV40
480 polyA sequence, was a gift of the laboratory of Lynn W. Enquist. Adeno-associated virus was
481 obtained from Addgene (https://www.addgene.org).

482 **IN VIVO VIRUS INJECTIONS**

483 **Surgery for HSV and PRV injections.** Mice were injected intraperitoneally with 15% mannitol
484 in 0.9% saline (M4125, Sigma-Aldrich, St. Louis, MO) approximately 30 minutes before surgery
485 to decrease surgical bleeding and facilitate viral uptake. Mice were then anesthetized with
486 isoflurane (5% induction, 1-2% isoflurane/oxygen maintenance vol/vol), eyes covered with
487 ophthalmic ointment (Puralube, Pharmaderm Florham Park, NJ), and stereotactically stabilized
488 (Kopf Model 1900, David Kopf Instruments, Tujunga, CA). After shaving hair over the scalp, a
489 midline incision was made to expose the posterior skull. Posterior neck muscles attaching to the
490 skull were removed, and the brain was exposed by making a craniotomy using a 0.5 mm micro-
491 drill burr (Fine Science Tools, Foster City, CA). External cerebellar vasculature was used to
492 identify cerebellar lobule boundaries to determine nominal anatomical locations for injection.
493 Injection pipettes were pulled from soda lime glass (71900-10 Kimble, Vineland, NJ) on a P-97

494 puller (Sutter Instruments, Novato, CA), beveled to 30 degrees with an approximate 10 µm tip
495 width, and backfilled with injection solution.

496 **AAV injections.** During stereotaxic surgery, mice were anesthetized with isoflurane (PCH,
497 induction: 5%; maintenance: 2.0-2.5%) and received a mannitol injection ntraperitoneally (2.33
498 g/kg in milli-Q) and a Rimadyl injection subcutaneously (5 mg/kg Carprofen 50 mg/ml, Pfizer,
499 Eurovet, in NaCl).. Body temperature was kept constant at 37°C with a feedback measurement
500 system (DC Temperature Control System, FHC, Bowdoin, ME, VS). Mice were placed into a
501 stereotactic frame (Stoelting, Chicago laboratory supply), fixing the head with stub ear bars and
502 a tooth bar. DURATEARS® eye ointment (Alcon) was used to prevent corneal dehydration. A 2
503 cm sagittal scalp incision was made, after which the exposed skull was cleaned with sterile
504 saline. Mice were given 2 small (Ø±1 mm) craniotomies in the interparietal bone (-2 mm AP
505 relative to lambda; 1.8 mm ML) for virus injection. Craniotomies were performed using a hand
506 drill (Marathon N7 Dental Micro Motor). A bilateral injection of AAV5-Syn-ChR2-eYFP (125 nl
507 per hemisphere, infusion speed ~0.05 µl/minute) in the AIN was done using a glass micropipette
508 controlled by a syringe. After slowly lowering the micropipette to the target site (2.2 mm ventral),
509 the micropipette remained stationary for 5 minutes before the start of the injection, and again
510 after finishing the injection. Micropipette was then withdrawn slowly from the brain (ejection
511 speed ~1 mm/minute). Craniotomies and skin were closed and mice received post-op Rimadyl.
512 Animals were perfused transcardially 3 weeks after viral injection using 4% PFA. Brains were
513 collected post mortem, stained for co-stained for DAPI (0100-20, Southern Biotech, Birmingham
514 AL), coronally sectioned at 40 µm/slice and imaged with an epifluorescent microscope at 20x
515 (Nanozoomer, Hamamatsu, Shizuoka, Japan).

516 **Transsynaptic viral tracing for tissue clearing (H129 and Bartha).** Transsynaptic viral
517 tracing studies used male and female 8-12 week-old C57BL/6J mice (The Jackson Laboratory,
518 Bar Harbor, Maine). Injection solution was prepared by making a 9:1 dilution of virus stock to
519 0.5% cholera toxin B conjugated to Alexa Fluor 555 in saline (CTB-555, C22843, Sigma-Aldrich;
520 as per [61]). At the timepoints used CTB-555 persisted at the injection site. Pressure injections
521 delivered 80 to 240 nl into the target location. Pipettes were inserted perpendicular to tissue
522 surface to a depth of approximately 200 μm. **Table 3** describes injection parameters for each
523 type of experiment.

524 After viral injection, Rimadyl (0.2 ml, 50 mg/ml, Carprofen, Zoetis, Florham Park, NJ)
525 was delivered subcutaneously. At the end of the post-injection incubation period, animals were
526 overdosed by intraperitoneal injection of ketamine/xylazine (ketamine: 400 mg/kg, Zetamine,
527 Vet One, ANADA #200-055; xylazine: 50 mg/kg, AnaSed Injection Xylazine, Akorn, NADA #139-
528 236) and transcardially perfused with 10 ml of 0.1 M phosphate buffer saline (PBS) followed by
529 25 ml 10% formalin (Fisher Scientific 23-245685). Tissue was fixed overnight in 10% formalin
530 before the iDISCO+ clearing protocol began.

531 For anterograde transport experiments, incubation times were determined by
532 immunostaining for viral antigens at various timepoints (30, 36, 41, 49, 54, 58, 67, 73, 80, 82
533 and 89 hours post-injection) the canonical ascending pathway of cerebellar cortex to deep
534 cerebellar nuclei to thalamus to neocortex. For retrograde transport experiments, incubation
535 times were determined by immunostaining for GFP (48, 60, 72, 78, 81, 84 and 91 hpi) targeting
536 the canonical descending pathway: neocortex to brainstem to cerebellar cortex. We selected
537 timepoints with the goal of achieving sufficient labeling for detection, while minimizing incubation
538 periods, given that with increasing long distance, transport time is increasingly dominated by
539 axon-associated transport mechanisms[54,62–64], leading to labeling of alternative paths and
540 retrograde paths after 96 hours[57].

541 **VIRAL TRACING WITH TISSUE SECTIONING AND SLIDE-BASED MICROSCOPY**

542 **Viral tracing by with classical sectioning-based histology: HSV-772 cerebellar injections.**
543 Adult Thy1-YFP male mice (YFP +, n=2, B6.Cg-Tg(Thy1-YFP)HJrs/J, 003782, The Jackson
544 Laboratory, 22 weeks), were prepared for surgery, in a similar fashion as in *Transsynaptic viral*
545 *tracing for tissue clearing (H129 and Bartha)*. We used the HSV recombinant HSV-772 (CMV-
546 EGFP, 9.02 x 10^8 PFU/ml; as in [57]), a H129 recombinant that produces a diffusible EGFP
547 reporter. Again, using a 9:1 HSV:CTB-555 injection solution, 350 nl/injection was pressure
548 injected into two mediolateral spots in lobule VIa. Eighty hours post-injection, animals were
549 overdosed using a ketamine/xylazine mixture as described previously. Brains were extracted
550 and fixed overnight in 10% formalin and cut at 50 μm thickness in PBS using a vibratome
551 (VT1000S, Leica). Sections were immunohistochemically blocked by incubating for 1 hour in
552 10% goat serum (G6767-100ML, Sigma-Aldrich, St. Louis, MO), 0.5% Triton X100 (T8787-
553 50ML, Sigma-Aldrich) in PBS. Next sections were put in primary antibody solution (1:750 Dako
554 Anti-HSV in 2% goat serum, 0.4% Triton X100 in PBS) for 72 hours at 4°C in the dark. Sections
555 were washed in PBS 4 times for 10 minutes each, and then incubated with secondary antibody
556 (1:300 Goat anti-rabbit-AF647 in 2% goat serum, 0.4% Triton X100 in PBS) for two hours.
557 Another series of PBS washes (four times, 10 minutes each) before mounting onto glass
558 microscope slides with vectashield mounting agent (H-1000, Vector Laboratories, Burlingame,
559 CA). Sections were fluorescently imaged at 20x (Nanozoomer, Hamamatsu, Shizuoka, Japan)
560 and at 63x with 5 μm z steps (Leica SP8 confocal laser-scanning microscope).

561 **TISSUE CLEARING AND LIGHT-SHEET MICROSCOPY**

562 **iDISCO+ tissue clearing.** After extraction, brains were immersed overnight in 10% formalin. An
563 iDISCO+ tissue clearing protocol[19] was used (*Supplementary Clearing Worksheet*). Brains were
564 dehydrated step-wise in increasing concentrations of methanol (Carolina Biological Supply,

565 874195; 20, 40, 60, 80, 100% in doubly distilled H20 (ddH20), 1 hr each), bleached in 5%
566 hydrogen peroxide/methanol solution (Sigma, H1009-100ML) overnight, and serially rehydrated
567 (methanol: ddH20 100, 80, 60, 40, 20%, 1 hr each). Brains were washed in 0.2% Triton X-100
568 (Sigma, T8787-50ML) in PBS, then in 20% DMSO (Fisher Scientific D128-1) + 0.3 M glycine
569 (Sigma 410225-50G) + 0.2% Triton X-100/PBS at 37°C for 2 days. Brains were then immersed
570 in a blocking solution of 10% DMSO + 6% donkey serum (EMD Millipore S30-100ml) + 0.2%
571 Triton X-100 + PBS at 37°C for 2-3 days to reduce non-specific antibody binding. Brains were
572 then twice washed for 1 hr/wash in PBS + 0.2% Tween-20 (Sigma P9416-50ML) + 10 μg/ml
573 heparin (Sigma H3149-100KU) (PTwH).
574 For HSV and c-Fos antibody labeling, brains were incubated with primary antibody
575 solution (see **Table 3** for antibody concentrations) consisting of 5% DMSO + 3% donkey serum
576 + PTwH at 37°C for 7 days. Brains were then washed in PTwH at least 5 times (wash intervals:
577 10 min, 15, 30, 1 hr, 2 hr), immunostained with secondary antibody in 3% donkey serum/PTwH
578 at 37°C for 7 days, and washed again in PTwH at least 5 times (wash intervals: 10 min, 15, 30,
579 1 hr, 2 hr). Finally, brains were serially dehydrated (methanol: ddH20: 100, 80, 60, 40, 20%, 1 hr
580 each), treated with 2:1 dichloromethane (DCM; Sigma, 270997-2L):methanol and then 100%
581 DCM, and placed in the refractive index matching solution dibenzyl ether (DBE; Sigma, 108014-
582 1KG) for storage at room temperature before imaging.

583 **Light-sheet microscopy for transsynaptic tracing.** Cleared brain samples were glued
584 (Loctite, 234796) ventral side down on a custom-designed 3D-printed holder and imaged in an
585 index-matched solution, DBE, using a light-sheet microscope (Ultramicroscope II, LaVision
586 Biotec., Bielefeld, Germany). Version 5.1.347 of the ImSpector Microscope controller software
587 was used. An autofluorescent channel for registration purposes was acquired using 488 nm
588 laser diode excitation and 525 nm emission (FF01-525/39-25, Semrock, Rochester, New York).
589 Injection sites, identified by CTB-555, were acquired at 561 nm excitation and 609 nm emission

590 (FF01-609/54-25, Semrock). Cellular imaging of virally infected cells (anti-HSV Dako B011402-
591 2) was acquired using 640 nm excitation and 680 nm emission (FF01-680/42-25, Semrock).
592 Cellular-resolution imaging was done at 1.63 μm/pixel (1x magnification, 4x objective, 0.28 NA,
593 5.6 - 6.0 mm working distance, 3.5 mm x 4.1 mm field of view, LVMI-FLuor 4x, LaVision
594 Biotech) with 3x3 tiling (with typically 10% overlap) per horizontal plane. Separate left- and right-
595 sided illumination images were taken every 7.5 micrometers step size using a 0.008 excitation-
596 sheet NA. A computational stitching approach[65] was performed independently for left- and right-
597 side illuminated volumes, followed by midline sigmoidal-blending of the two volumes to reduce
598 movement and image artifacts.

599 **REGISTRATION AND ATLAS PREPARATION**

600 **Image registration.** Most registration software cannot compute transformation with full-sized
601 light-sheet volumes in the 100-200 gigabyte range due to computational limits. Using mid-range
602 computers, reasonable processing times are obtained with file sizes of 300-750 megabytes,
603 which for mouse brain corresponds to 20 μm/voxel. Empirically, we found that light-sheet brain
604 volumes to be aligned ("moving") resampled to approximately 140% the size of the reference
605 ("fixed") atlas volume yielded the best registration performance. Alignment was done by
606 applying an affine transformations allowing for translation, rotation, shearing and scaling to
607 generally align with the atlas, followed by b-spline transformation to account for brain-subregion
608 variability among individual brains.

609 For uniformity among samples, registration was done using the autofluorescence
610 channel, which has substantial autofluorescence at shorter wavelengths useful for registration[66].
611 In addition to autofluorescence-to-atlas registration, the signal channel was registered using an
612 affine transformation to the autofluorescence channel to control for minor brain movement
613 during acquisition, wavelength-dependent aberrations, and differences in imaging parameters[19].

Affine and b-spline transformations were computed using elastix[67,68]; see supplemental Elastix affine and b-spline parameters used for light-sheet volume registration. Briefly, the elastix affine transform allows for translation (t), rotation (R), shearing (G), and scaling (S) and is defined as:

$$\boldsymbol{T_\mu}(\boldsymbol{x}) = \boldsymbol{RGS}(\boldsymbol{x} - \boldsymbol{c}) + \boldsymbol{t} + \boldsymbol{c}$$

where c is a center of rotation and t is a translation. The elastix b-spline transformation allows for nonlinearities and is defined as:

$$\boldsymbol{T_\mu}(\boldsymbol{x}) = \boldsymbol{x} + \sum_{\boldsymbol{x}_k \in \mathcal{N}_{\boldsymbol{x}}} \boldsymbol{p}_k \boldsymbol{\beta}^3 \left(\frac{\boldsymbol{x} - \boldsymbol{x}_k}{\boldsymbol{\sigma}} \right)$$

Where x_κ are control points, $\beta^3(x)$ the B-spline polynomial, p_κ the b-spline coefficient vectors, Nx, B-spline compact support control points, and σ is the b-spline compact control point-spacing (see [69], pages 8-10 for reference). For the assignment of cell centers to anatomical locations, we calculated transformations from cell signal space to autofluorescent space (affine only) and autofluorescent space to atlas space (affine and b-spline; **Supplementary Figure 13**).

Princeton Mouse Atlas generation. To generate a light-sheet atlas with a complete posterior cerebellum, autofluorescent light-sheet volumes from 110 mice (curated to eliminate distortions related to damage, clearing, or imaging) were resampled to an isotropic 20 μm per voxel resolution (**Figure 2; Supplementary Figure 1a**). We selected a single brain volume to use as the fixed (template) volume for registration of the other 109 brains and computed the transformations between the other 109 brains and the template brain. The registration task was parallelized from ClearMap[19] adapting code for use on a Slurm-based[70] computing cluster.

After registration, all brains were pooled into a four-dimensional volume (brain, x, y, z), and the median voxel value at each xyz location was used to generate a single median three-

636 dimensional volume. Flocculi and paraflocculi, which can become damaged or deformed during
637 extraction and clearing, were imaged separately from a subset of 26 brains in which these
638 structures were intact and undeformed. Manual voxel curation sharpened brain-edges in areas
639 where pixel intensity gradually faded. Finally, contrast limited adaptive histogram equalization
640 (skimage.exposure.equalize_adapthist) applied to the resulting volume increased local contrast
641 within brain structures, generating the final PMA (**Supplementary Figure 1b; Supplementary**
642 **Figure 14**). We then determined the transformation between the PMA and the Allen Brain
643 CCFv3[71] space in order to maintain translatability. Our software for basic atlas creation with an
644 accompanying Jupyter tutorial notebook is available online via
645 github.com/PrincetonUniversity/pytlas. Volumetric projection renderings were made using
646 ImageJ[72]; 3D project function (**Supplementary Figure 1a**).

647 **Statistical analysis of registration precision**. Precision of registration was measured by
648 quantifying euclidean landmark distances, defined by blinded users (similar to [73]) between the
649 PMA and brains at different stages of registration. Estimated standard deviations are defined as
650 the median absolute deviation (MAD) divided by 0.6745. MADs were calculated with
651 Statsmodels[74] 0.9.0 (statsmodels.robust.mad). One measurement was considered to be user
652 error and was dropped in the theoretical-limit measurements, as it was over 12 times the
653 median of the other measures.

654 **Generation of 3D printable files.** To generate 3D printable Princeton Mouse Atlas files usable
655 for experimental and educational purposes, we loaded volumetric tiff files as surface objects
656 using the ImageJ-based 3D viewer. After resampling by a factor of 2 and intensity thresholding,
657 data were then imported to Blender[75], where surfaces were smoothed (Smooth Vertex tool)
658 before finally exporting as stereolithography (stl) files.

659 **AUTOMATED DETECTION OF VIRALLY LABELED CELLS**

660 **BrainPipe, an automated transsynaptic tracing and labeling analysis pipeline.** Whole-brain
661 light-sheet volumes were analyzed using a new pipeline, BrainPipe. BrainPipe consists of three
662 steps: cell detection, registration to a common atlas, and injection site recovery. For maximum
663 detection accuracy, cell detection was performed on unregistered image volumes, and the
664 detected cells were then transformed to atlas coordinates.

665 Before analysis, datasets were manually curated by stringent quality control standards.
666 Each brain was screened for (1) clearing quality, (2) significant tissue deformation from
667 extraction process, (3) viral spread from injection site, (4) antibody penetration, (5) blending
668 artifacts related to microscope misalignment, (6) injection site within target location, (7)
669 successful registration, and (8) CNN overlay of detected cells with brain volume in signal
670 channel. Because of the relatively high concentration of antibody solution needed for brain-wide
671 immunohistochemical staining, non-specific fluorescence was apparent at the edges of tissue,
672 i.e. outside of the brain and ventricles, in the form of punctate labeling not of cell origin. We
673 computationally removed a border at the brain edge at the ventricles to remove false positives,
674 at the cost of loss of some true positives (skimage.morphology.binary_erosion, **Table 4**). For
675 neocortical layer studies, a subregion of the primary somatosensory area: "primary
676 somatosensory area, unassigned" in PMA did not have layer-specific mapping in Allen Atlas
677 space and was removed from consideration.

678 **Injection site recovery and cell detection.** Injection sites were identified in H129 studies by
679 co-injecting CTB with virus (**Supplementary Figure 15**) and in c-Fos studies using ArchT-GFP
680 expression. Post-registered light-sheet volumes of the injection channel were segmented to
681 obtain voxel-by-voxel injection-site reconstructions. Volumes were Gaussian blurred (3 voxels).
682 All voxels below 3 standard deviations above the mean were removed. The single largest
683 connected component was considered the injection site (scipy.ndimage.label, SciPy 1.1.0[76]).

684 CTB was selected for injection site labelling for transsynaptic tracing as it does not affect the
685 spread of alpha-herpesviruses and its greater diffusion due to its smaller size overestimates the
686 viral injection size by as much as two-fold[77,78]. CTB overestimates the viral spread during
687 injection, due to its lower molecular weight compared with H129. **Supplementary Figure 16**
688 shows the percentage of cerebellum covered by at least one injection in each of the three
689 datasets. Lobules I-III, flocculus, and paraflocculus were not targeted.

690 **Automated detection of transsynaptically labeled neurons.**

691 To optimize cell detection for scalability, whole-brain light-sheet volumes (typically 100-150 GB
692 16-bit volumes) were chunked into approximately 80 compressed 32-bit TIF volumes per brain,
693 with an overlap of 192 x 192 x 20 voxels in xyz between each volume, and stored on a file
694 server.

695 For deploying the custom-trained cell-detection neural network, the file server streamed
696 the volumes to a GPU cluster for segmentation. Once the segmentation was completed, the
697 soma labels were reconstructed across the entire brain volume from the segmented image on a
698 CPU cluster by calculating the maximum between the overlapping segments of each volume.
699 The reconstructed brain volumes after segmentation were stored as memory-mapped arrays on
700 a file server. Coordinates of cell centers from the reconstructed volumes were obtained by
701 thresholding, using the established threshold from training evaluation, and connected-
702 component analysis. Additionally, measures of detected cell perimeter, sphericity, and number
703 of voxels it spans in the z-dimension were calculated by connected-component analysis for
704 further cell classification if needed. The final output consisted of a comma-separated values file
705 that includes the xyz coordinates as well as measures of perimeter, sphericity, and number of
706 voxels in the z-dimension for each detected cell in the brain volume.

707 **Convolutional neural network training**. Supervised learning using CNN is useful in complex
708 classification tasks when a sufficient amount of training data is available. Annotated training
709 volumes were generated by selecting volumes at least 200 x 200 x 50 pixels (XYZ) from full-
710 sized cell channel volumes. To ensure training data were representative of the animal variability
711 across the whole-brain, training volumes were selected from different anatomical regions in
712 different brains with various amounts of labeling (see **Table 1** for dataset description).
713 Annotations were recorded by marking cell centers using ImageJ[72]. To generate labeled
714 volumes, Otsu's thresholding method (skimage.filters.threshold_otsu, Scikit-Image[79] 0.13.1) was
715 applied within windows (30 x 30 x 8 voxels, XYZ) around each center to label soma. Using
716 annotated volumes, we trained a three-dimensional CNN with a U-Net architecture[80,81]
717 (github.com/PrincetonUniversity/BrainPipe). A 192 x 192 x 20 CNN window size with 0.75
718 strides was selected. The training dataset was split into a 70% training, 20% validation, and
719 10% testing subset. Training occurred on a SLURM-based GPU cluster. During training, the
720 CNN was presented with data from the training dataset, and after each iteration its performance
721 was evaluated using the validation dataset. Loss values, which measure learning by the CNN,
722 stabilized at 295,000 training iterations, at which point training was stopped and the CNN was
723 evaluated for performance, as a risk in machine learning is overfitting, i.e. the possibility that the
724 neural network will learn particular training examples rather than learning the category.

725 **Evaluation of CNN.** To determine CNN performance on H129 data, we calculated an F1 score
726 [82]. First, we needed to compare CNN output with our ground truth annotations by quantifying
727 true positives (TP), false negatives (FN), and false positives (FP). Our neural network
728 architecture produced a voxel-wise 0 (background) to 1 (cell) probability output. To determine a
729 threshold value for binarization of the continuous 0-1 CNN-output values, F1 scores as a
730 function of thresholds between 0 and 1 were determined (**FIgure 1f**). Connected-component
731 analysis (scipy.ndimage.label) grouped islands of nonzero voxels to identify each island as a

732 putative cell. Pairwise Euclidean distances (scipy.spatial.distance.euclidean) were calculated
733 between CNN-predicted cell centers and human-annotated ground truth centers. Bipartite
734 matching serially paired closest predicted and ground truth centers, removing each from
735 unpaired pools. Unmatched predicted or ground truth centers were considered FPs or FNs,
736 respectively. Prediction-ground truth center pairs with a Euclidean distance greater than 30
737 voxels (~49 μm) were likely inaccurate and not paired.

738 The F1 score was defined as the harmonic average of precision and recall. Precision is
739 the number of correct positive results divided by the number of all positive results returned by
740 the classifier, i.e. TP/(TP+FP). Recall is the number of correct positive results divided by the
741 number of all samples that should have been identified as positive, i.e. TP/(TP+FN). The F1
742 score reaches its best value at 1 (perfect precision and recall) and worst at 0. Using a 20 voxel
743 cutoff instead of 30 gave 0.849 and 0.875 for human-CNN and human-human F1 scores,
744 respectively. To determine CNN performance metrics, the testing dataset, which the network
745 had yet to be exposed to was finally run using the established threshold producing an F1 score
746 of 0.864. To generate the precision-recall curve, precision and recall values were calculated
747 between thresholds of 0.002 and 0.998 with a step size of 0.002. Values of precision and 1-
748 recall were used to plot the curve. The area-under-curve of the precision-recall curve was
749 calculated using the composite trapezoidal rule (numpy.trapz).

750 **Statistical analysis of transsynaptic tracing data.** For initial inspection of thalamic or
751 neocortical neurons, each injected brain was sorted by cerebellar region with the greatest
752 volume fraction of the injection (as in [2]; this region was defined as the primary injection site.
753 Injections from each “primary” region were then pooled and averaged per thalamic nucleus
754 (**Figure 3f**).

755 **Generalized linear model analysis.** Contribution of each cerebellar meta-lobule to viral spread
756 in each neocortical or thalamic region was fitted to a generalized linear model (GLM) consisting
757 of an inhomogeneous Poisson process as a function of seven targeted cerebellar regions
758 ("meta-lobules"). The predictor variables were x_j, where x_j is defined as the fraction of the total
759 injection to be found in the j-th meta-lobule, such that $\Sigma\, x_j = 1$. The outputs to be predicted were
760 y_k defined as the fraction of the total number of cells in the entire neocortex (or thalamus) to be
761 found in the k-th region. For the resulting fit coefficients β_{jk}, the change in $\hat{y}_k$ arising from a unit
762 change in x_j is $e^{\beta_{jk}} - 1$. In **figures 3f**, **5f,** and **7f,** the heatmap indicates a measure of
763 confidence, defined as the coefficient (β_{jk}) divided by the coefficient's standard error.
764 To determine greater than chance significant weights, we compared significant weights
765 computed from the t-stats of the coefficients with those observed in a shuffle-based null model
766 in which predictors were shuffled uniformly at random (n = 1,000). We found that the true
767 number of positive significant weights is significantly greater than that expected under the null
768 model with a one-sided, non-parametric $p < 0.05$. In **Figure 7**, the neocortical region "Frontal
769 pole, cerebral cortex" was excluded from generalized linear model analysis due to zero counts
770 across all brains for the region.

771 **C-FOS MAPPING EXPERIMENT**

772 **c-Fos mapping after optogenetic perturbation.** Neural activity has been shown to increase c-
773 Fos, an immediate-early gene product[83]. Mapping of c-Fos expression used L7-Cre +/- (n=10)
774 and -/- (n=8) mice (males, B6; 129-Tg(Pcp2-cre)2Mpin/J, 004146, The Jackson Laboratory, Bar
775 Harbor, Maine, bred in-house, 56 days or older). L7-Cre mice express Cre recombinase
776 exclusively in Purkinje neurons[84]. rAAV1-CAG-FLEX-ArchT-GFP (UNC Vector Core, deposited
777 by Dr. Ed Boyden, 4×10^{12} vg/ml, AV5593B lot number, 500 nl/injection 250 μm deep
778 perpendicular to tissue) was pressure injected into four locations in lobule VIa/b. After virus

779 injection, a cover slip (round 3 mm, #1 thickness, Warner Instruments 64–0720) was used to
780 cover the craniotomy and a custom titanium plate for head fixation[85] was attached using dental
781 cement (S396, Parkell, Brentwood, NY). Mice were allowed to recover after surgery for 4 weeks
782 and then were habituated to a head-fixed treadmill[85] for three days, 30 minutes per day. On the
783 last day of habituation, ArchT-GFP expression was confirmed using wide-field fluorescence
784 microscopy. The following day, mice were again placed on the treadmill and a 200 μm fiber
785 (M200L02S-A, Thorlabs, Newton, NJ) was placed directly over the cranial window for
786 optogenetic stimulation with 532 nm laser (1 Hz, 250 ms pulse-width, 56 mW, 1 hr, GR-532-
787 00200-CWM-SD-05-LED-0, Opto Engine, Midvale, UT). Mice were then individually placed into
788 a clean cage, kept in the dark for one hour, and perfused as described previously. Brains were
789 fixed overnight in 10% formalin (4% formaldehyde) before beginning the iDISCO+ clearing
790 protocol (**Table 1**). Both ArchT-expressing mice and non-expressing mice received cranial
791 windows, habituation, and photostimulation.

792 **Electrophysiological confirmation of ArchT expression in Purkinje cells.** To confirm that
793 ArchT was optically activatable in Purkinje cells, photostimulation was done during patch clamp
794 recording in acutely prepared brain slices. Brain slices were prepared from three 10 week-old
795 male Pcp2-cre mice (B6.Cg-Tg(Pcp2-cre)3555Jdhu/J, 010536, The Jackson Laboratory), two
796 weeks after injection with rAAV1-CAG-FLEX-ArchT-GFP. Mice were deeply anesthetized with
797 Euthasol (0.06 ml/30g), decapitated, and the brain removed. The isolated whole brains were
798 immersed in ice-cold carbogenated NMDG ACSF solution (92 mM N-methyl D-glucamine, 2.5
799 mM KCl, 1.25 mM NaH_2PO_4, 30 mM $NaHCO_3$, 20 mM HEPES, 25 mM glucose, 2 mM thiourea,
800 5 mM Na-ascorbate, 3 mM Na-pyruvate, 0.5 mM $CaCl_2$, 10 mM $MgSO_4$, and 12 mM N-acetyl-L-
801 cysteine, pH adjusted to 7.3–7.4). Parasagittal cerebellar brain slices 300 μm) were cut using a
802 vibratome (VT1200s, Leica Microsystems, Wetzlar, Germany), incubated in NMDG ACSF at
803 34°C for 15 minutes, and transferred into a holding solution of HEPES ACSF (92 mM NaCl, 2.5

804 mM KCl, 1.25 mM NaH_2PO_4, 30 mM $NaHCO_3$, 20 mM HEPES, 25 mM glucose, 2 mM thiourea,
805 5 mM Na-ascorbate, 3 mM Na-pyruvate, 2 mM $CaCl_2$, 2 mM $MgSO_4$ and 12 mM N-acetyl-L-
806 cysteine, bubbled at room temperature with 95% O_2 and 5% CO_2). During recordings, slices
807 were perfused at a flow rate of 4–5 ml/min with a recording ACSF solution (120 mM NaCl, 3.5
808 mM KCl, 1.25 mM NaH_2PO_4, 26 mM $NaHCO_3$, 1.3 mM $MgCl_2$, 2 mM $CaCl_2$ and 11 mM D-
809 glucose) and continuously bubbled with 95% O_2 and 5% CO_2.
810 Whole-cell recordings were performed using a Multiclamp 700B (Molecular Devices,
811 Sunnyvale, CA) using pipettes with a resistance of 3–5 MΩ filled with a potassium-based
812 internal solution (120 mM potassium gluconate, 0.2 mM EGTA, 10 mM HEPES, 5 mM NaCl, 1
813 mM $MgCl_2$, 2 mM Mg-ATP and 0.3 mM Na-GTP, pH adjusted to 7.2 with KOH). Purkinje
814 neurons expressing YFP were selected for recordings. Photostimulation parameters used were
815 525 nm, 0.12 mW/mm², and 250 ms pulses at 1 Hz.

816 **Light-sheet microscopy for c-Fos imaging.** Opaque magnets (D1005A-10 Parylene,
817 Supermagnetman, Pelham, AL) were glued to ventral brain surfaces in the horizontal orientation
818 and imaged using a light-sheet microscope as described previously. Version 5.1.293 of the
819 ImSpector Microscope controller software was used. ArchT-GFP injection volumes were
820 acquired using the 561 nm excitation filter. Cellular imaging of c-Fos expressing cells was
821 acquired using 640 nm excitation filter at 5.0 μm/pixel (1x magnification, 1.3x objective, 0.1
822 numerical aperture, 9.0 mm working distance, 12.0 x 12.0 mm field of view, LVMI-Fluor 1.3x,
823 LaVision Biotech) with a 3 μm step-size using a 0.010 excitation NA. This resolution was
824 selected to allow whole-brain imaging using ClearMap without tiling artifacts. To speed up
825 acquisitions, the autofluorescence channel and injection channels were acquired separately with
826 a shorter exposure time than the cell channel. The left and right horizontal focus was shifted
827 towards the side of the emitting sheet. Left and right images were then sigmoidally blended

828 before analysis. In order to maximize field of view, some olfactory areas were not completely
829 represented in images and were removed from analysis. Five brains were reimaged a second
830 time due to ventricular imaging artifacts.

831 **Automated detection of c-Fos expressing cells.** Detection of c-Fos expressing cells after
832 optogenetic stimulation was done using ClearMap software for c-Fos detection[19] modified to run
833 on high performance computing clusters ("ClearMapCluster", see **Table 5** for analysis
834 parameters). Cell detection parameters were optimized by two users iterating through a set of
835 varying ClearMap detection parameters and selecting those that minimized false positives while
836 labelling only c-Fos positive neurons with high signal-to-noise ratio.

837 **Statistical analysis of c-Fos data.** Cell and density heat maps and p-value maps were
838 generated using ClearMap. Projected p-value maps were generated by binarizing the p-value
839 maps and counting non-zero voxels in z; color bar thresholding displayed greater than 25% for
840 coronal and 27% for sagittal sections of the z-distance. Injection sites were segmented and
841 aligned in the manner described previously. Activation ratio was defined as the mean number of
842 cells in an anatomical area across experimental brains divided by the mean number of cells in
843 the same anatomical area in control brains. To compare the c-Fos activation data with
844 transsynaptic tracing data across the major divisions in the neocortex, average viral-labeling
845 neocortical densities from brains with lobule-VIa H129-VC22 injections were compared with the
846 cell count ratio of c-Fos stimulation vs control groups by performing a rank order regression
847 (scipy.stats.kendalltau).

SOFTWARE

Data analysis pipelines were run using custom code written for Python 3+ (available at github.com/PrincetonUniversity/BrainPipe and github.com/PrincetonUniversity/ClearMapCluster)

Unless otherwise noted, analyses and plotting were performed in Python 2.7+. DataFrame manipulations were done using Numpy[86] 1.14.3 and Pandas[87] 0.23.0. Plotting was done with Matplotlib[88] 2.2.2 and Seaborn[89] 0.9.0. Image loading, manipulation and visualization was done using Scikit-Image[79] 0.13.1 and SimpleITK[90] 1.0.0. SciPy[76] 1.1.0 was used for statistical analyses. Clustering analysis was performed using Seaborn[89] 0.9.0 and Scikit-Learn[91] 0.19.1 was used for hierarchical agglomerative clustering (average metric, Ward's method). Coefficients and standard errors for the generalized linear model were obtained by fitting the model using the statsmodels 0.9.0 package in Python 3.7.1 (as [2]). The Mann-Whitney U test (two-tailed; scipy.stats.mannwhitneyu, SciPy[76] 1.1.0) was used to determine statistical significance between control and experimental brain regions in c-Fos studies.

ACKNOWLEDGMENTS

We thank Aleksandra Badura for advice on experimental design, Lynn W. Enquist for discussion and for the generous gift of PRV-Bartha 152 (CNNV, P40 OD010996), James Gornet for neural network implementation assistance, Austin Hoag for software design and management, Nicolas Renier and Kelly Seagraves for tissue clearing optimization, Stephan Thiberge for microscopy help, and Shruthi Deivasigamani, Joseph Gotto, Joyce C. Lee, Laura Lynch, Dafina Pacuku, and Thaddeus Weigel for technical assistance. This work was supported by NIH R01 NS045193, R01 MH115750, and U19 NS104648 (S.W.), F31 NS089303 (T.P.), Netherlands Organization for Scientific Research - Veni ZonMW, 91618112 (H.J.B), Erasmus MC Fellowship 106958 (H.J.B), and the New Jersey Council on Brain Injury Research (J.V.).

AUTHOR CONTRIBUTIONS

T.P., M.K., H.-J.B., and S.W. conceived and designed the experiments. T.P., D.B., and J.V. performed virus injections and prepared tissue. Z.D. and T.P. imaged tissue and ran the computational data analysis pipeline for whole-brain imaging data. T.P., Z.D., and H.-J. B. performed subsequent data analysis and prepared figures. E.E. designed and provided HSV vectors. K.V. and T.P. designed algorithms for image analysis. M.K.., J.L., and T.P. performed optogenetics experiments. H.-J. B. and N. de O. performed AAV experiments and collected and analyzed images. T.P. and S.W. wrote the initial draft of the manuscript, which was edited by all authors.

COMPETING INTERESTS

The authors declare that they have no competing interests.

882 **REFERENCES**

883 1. Stoodley, C. J. & Schmahmann, J. D. Functional topography in the human cerebellum: a
884 meta-analysis of neuroimaging studies. *Neuroimage* **44**, 489–501 (2009)
885 doi:10.1016/j.neuroimage.2008.08.039.
886 2. Badura, A. *et al.* Normal cognitive and social development require posterior cerebellar
887 activity. *Elife* **7**, (2018) doi:10.7554/eLife.36401.
888 3. Deverett, B., Koay, S. A., Oostland, M. & Wang, S. S.-H. Cerebellar involvement in an
889 evidence-accumulation decision-making task. *Elife* **7**, (2018) doi:10.7554/eLife.36781.
890 4. Courchesne, E. *et al.* Unusual brain growth patterns in early life in patients with autistic
891 disorder: an MRI study. *Neurology* **57**, 245–254 (2001).
892 5. Limperopoulos, C. *et al.* Does cerebellar injury in premature infants contribute to the high
893 prevalence of long-term cognitive, learning, and behavioral disability in survivors?
894 *Pediatrics* **120**, 584–593 (2007) doi:10.1542/peds.2007-1041.
895 6. Wang, S. S.-H., Kloth, A. D. & Badura, A. The cerebellum, sensitive periods, and autism.
896 *Neuron* **83**, 518–532 (2014) doi:10.1016/j.neuron.2014.07.016.
897 7. Wagner, M. J. & Luo, L. Neocortex-Cerebellum Circuits for Cognitive Processing. *Trends*
898 *Neurosci.* (2019) doi:10.1016/j.tins.2019.11.002.
899 8. Clark, D. A., Mitra, P. P. & Wang, S. S.-H. Scalable architecture in mammalian brains.
900 *Nature* **411**, 189–193 (2001) doi:10.1038/35075564.
901 9. Voogd, J. & Ruigrok, T. J. H. Chapter 15 - Cerebellum and Precerebellar Nuclei. in *The*
902 *Human Nervous System (Third Edition)* (eds. Mai, J. K. & Paxinos, G.) 471–545 (Academic
903 Press, 2012). doi:10.1016/B978-0-12-374236-0.10015-X.
904 10. Percheron, G., François, C., Talbi, B., Yelnik, J. & Fénelon, G. The primate motor thalamus.
905 *Brain Res. Brain Res. Rev.* **22**, 93–181 (1996).
906 11. Ruigrok, T. J. H., Sillitoe, R. V. & Voogd, J. Chapter 9 - Cerebellum and Cerebellar
907 Connections. in *The Rat Nervous System (Fourth Edition)* (ed. Paxinos, G.) 133–205

908 (Academic Press, 2015). doi:10.1016/B978-0-12-374245-2.00009-7.
909 12. Carta, I., Chen, C. H., Schott, A. L., Dorizan, S. & Khodakhah, K. Cerebellar modulation of
910 the reward circuitry and social behavior. *Science* **363**, (2019) doi:10.1126/science.aav0581.
911 13. Strick, P. L., Dum, R. P. & Fiez, J. A. Cerebellum and nonmotor function. *Annu. Rev.*
912 *Neurosci.* **32**, 413–434 (2009) doi:10.1146/annurev.neuro.31.060407.125606.
913 14. Popa, T., Russo, M. & Meunier, S. Long-lasting inhibition of cerebellar output. *Brain Stimul.*
914 **3**, 161–169 (2010) doi:10.1016/j.brs.2009.10.001.
915 15. Schutter, D. J. L. G. & van Honk, J. An electrophysiological link between the cerebellum,
916 cognition and emotion: frontal theta EEG activity to single-pulse cerebellar TMS.
917 *Neuroimage* **33**, 1227–1231 (2006) doi:10.1016/j.neuroimage.2006.06.055.
918 16. Buckner, R. L., Krienen, F. M., Castellanos, A., Diaz, J. C. & Yeo, B. T. T. The organization
919 of the human cerebellum estimated by intrinsic functional connectivity. *J. Neurophysiol.*
920 **106**, 2322–2345 (2011) doi:10.1152/jn.00339.2011.
921 17. Choe, K. Y., Sanchez, C. F., Harris, N. G., Otis, T. S. & Mathews, P. J. Optogenetic fMRI
922 and electrophysiological identification of region-specific connectivity between the cerebellar
923 cortex and forebrain. *Neuroimage* **173**, 370–383 (2018)
924 doi:10.1016/j.neuroimage.2018.02.047.
925 18. Dum, R. P. & Strick, P. L. Transneuronal tracing with neurotropic viruses reveals network
926 macroarchitecture. *Curr. Opin. Neurobiol.* **23**, 245–249 (2013)
927 doi:10.1016/j.conb.2012.12.002.
928 19. Renier, N. *et al.* Mapping of Brain Activity by Automated Volume Analysis of Immediate
929 Early Genes. *Cell* **165**, 1789–1802 (2016) doi:10.1016/j.cell.2016.05.007.
930 20. Teune, T. M., van der Burg, J., van der Moer, J., Voogd, J. & Ruigrok, T. J. Topography of
931 cerebellar nuclear projections to the brain stem in the rat. *Prog. Brain Res.* **124**, 141–172
932 (2000) doi:10.1016/S0079-6123(00)24014-4.
933 21. Aumann, T. D. & Horne, M. K. Ramification and termination of single axons in the

934 cerebellothalamic pathway of the rat. *J. Comp. Neurol.* **376**, 420–430 (1996) doi:3.0.CO;2-
935 4">10.1002/(SICI)1096-9861(19961216)376:3<420::AID-CNE5>3.0.CO;2-4.
936 22. Jones, E. G. *The Thalamus*. (Springer Science & Business Media, 2012).
937 23. Mitchell, A. & Chakraborty, S. What does the mediodorsal thalamus do? *Front. Syst.*
938 *Neurosci.* **7**, 37 (2013) doi:10.3389/fnsys.2013.00037.
939 24. Hunnicutt, B. J. *et al.* A comprehensive thalamocortical projection map at the mesoscopic
940 level. *Nat. Neurosci.* **17**, 1276–1285 (2014) doi:10.1038/nn.3780.
941 25. Courchesne, E., Yeung-Courchesne, R., Press, G. A., Hesselink, J. R. & Jernigan, T. L.
942 Hypoplasia of cerebellar vermal lobules VI and VII in autism. *N. Engl. J. Med.* **318**, 1349–
943 1354 (1988) doi:10.1056/NEJM198805263182102.
944 26. Watabe-Uchida, M., Zhu, L., Ogawa, S. K., Vamanrao, A. & Uchida, N. Whole-brain
945 mapping of direct inputs to midbrain dopamine neurons. *Neuron* **74**, 858–873 (2012)
946 doi:10.1016/j.neuron.2012.03.017.
947 27. Phillipson, O. T. Afferent projections to the ventral tegmental area of Tsai and
948 interfascicular nucleus: a horseradish peroxidase study in the rat. *J. Comp. Neurol.* **187**,
949 117–143 (1979) doi:10.1002/cne.901870108.
950 28. Snider, R. S. & Maiti, A. Cerebellar contributions to the Papez circuit. *J. Neurosci. Res.* **2**,
951 133–146 (1976) doi:10.1002/jnr.490020204.
952 29. Bostan, A. C. & Strick, P. L. The basal ganglia and the cerebellum: nodes in an integrated
953 network. *Nat. Rev. Neurosci.* **19**, 338–350 (2018) doi:10.1038/s41583-018-0002-7.
954 30. Yoshizawa, T., Ito, M. & Doya, K. Reward-Predictive Neural Activities in Striatal Striosome
955 Compartments. *eNeuro* **5**, (2018) doi:10.1523/ENEURO.0367-17.2018.
956 31. Stamatakis, A. M. *et al.* Lateral Hypothalamic Area Glutamatergic Neurons and Their
957 Projections to the Lateral Habenula Regulate Feeding and Reward. *J. Neurosci.* **36**, 302–
958 311 (2016) doi:10.1523/JNEUROSCI.1202-15.2016.
959 32. Lee, K. H. *et al.* Circuit mechanisms underlying motor memory formation in the cerebellum.

960 *Neuron* **86**, 529–540 (2015) doi:10.1016/j.neuron.2015.03.010.
961 33. Jones, E. G. & Burton, H. Areal differences in the laminar distribution of thalamic afferents
962 in cortical fields of the insular, parietal and temporal regions of primates. *J. Comp. Neurol.*
963 **168**, 197–247 (1976) doi:10.1002/cne.901680203.
964 34. Jones, E. G. Lamination and differential distribution of thalamic afferents within the sensory-
965 motor cortex of the squirrel monkey. *J. Comp. Neurol.* **160**, 167–203 (1975)
966 doi:10.1002/cne.901600203.
967 35. Herkenham, M. Laminar organization of thalamic projections to the rat neocortex. *Science*
968 **207**, 532–535 (1980) doi:10.1126/science.7352263.
969 36. Thomson, A. M. Neocortical layer 6, a review. *Front. Neuroanat.* **4**, 13 (2010)
970 doi:10.3389/fnana.2010.00013.
971 37. Wiesendanger, R. & Wiesendanger, M. The corticopontine system in the rat. I. Mapping of
972 corticopontine neurons. *J. Comp. Neurol.* **208**, 215–226 (1982)
973 doi:10.1002/cne.902080302.
974 38. Hashimoto, M. *et al.* Motor and non-motor projections from the cerebellum to rostrocaudally
975 distinct sectors of the dorsal premotor cortex in macaques. *Eur. J. Neurosci.* **31**, 1402–1413
976 (2010) doi:10.1111/j.1460-9568.2010.07151.x.
977 39. Asanuma, C., Thach, W. T. & Jones, E. G. Distribution of cerebellar terminations and their
978 relation to other afferent terminations in the ventral lateral thalamic region of the monkey.
979 *Brain Res. Rev.* **5**, 237–265 (1983) doi:10.1016/0165-0173(83)90015-2.
980 40. Hubel, D. H. & Wiesel, T. N. Binocular interaction in striate cortex of kittens reared with
981 artificial squint. *J. Neurophysiol.* **28**, 1041–1059 (1965) doi:10.1152/jn.1965.28.6.1041.
982 41. Salgado, S. & Kaplitt, M. G. The Nucleus Accumbens: A Comprehensive Review.
983 *Stereotact. Funct. Neurosurg.* **93**, 75–93 (2015) doi:10.1159/000368279.
984 42. Beier, K. T. *et al.* Circuit Architecture of VTA Dopamine Neurons Revealed by Systematic
985 Input-Output Mapping. *Cell* **162**, 622–634 (2015) doi:10.1016/j.cell.2015.07.015.

986 43. Küper, M. *et al.* Cerebellar fMRI Activation Increases with Increasing Working Memory
987 Demands. *Cerebellum* **15**, 322–335 (2016) doi:10.1007/s12311-015-0703-7.
988 44. Stoodley, C. J. *et al.* Altered cerebellar connectivity in autism and cerebellar-mediated
989 rescue of autism-related behaviors in mice. *Nat. Neurosci.* **20**, 1744–1751 (2017)
990 doi:10.1038/s41593-017-0004-1.
991 45. Ando, N., Izawa, Y. & Shinoda, Y. Relative contributions of thalamic reticular nucleus
992 neurons and intrinsic interneurons to inhibition of thalamic neurons projecting to the motor
993 cortex. *J. Neurophysiol.* **73**, 2470–2485 (1995) doi:10.1152/jn.1995.73.6.2470.
994 46. Cavdar, S. *et al.* Cerebellar connections to the rostral reticular nucleus of the thalamus in
995 the rat. *J. Anat.* **201**, 485–491 (2002) doi:10.1046/j.1469-7580.2002.00119.x.
996 47. Pinto, D. J., Brumberg, J. C. & Simons, D. J. Circuit dynamics and coding strategies in
997 rodent somatosensory cortex. *J. Neurophysiol.* **83**, 1158–1166 (2000)
998 doi:10.1152/jn.2000.83.3.1158.
999 48. Lam, Y.-W. & Sherman, S. M. Functional organization of the somatosensory cortical layer 6
1000 feedback to the thalamus. *Cereb. Cortex* **20**, 13–24 (2010) doi:10.1093/cercor/bhp077.
1001 49. Guillery, R. W., Feig, S. L. & Lozsádi, D. A. Paying attention to the thalamic reticular
1002 nucleus. *Trends Neurosci.* **21**, 28–32 (1998) doi:10.1016/S0166-2236(97)01157-0.
1003 50. Bruno, R. M. & Sakmann, B. Cortex is driven by weak but synchronously active
1004 thalamocortical synapses. *Science* **312**, 1622–1627 (2006) doi:10.1126/science.1124593.
1005 51. Destexhe, A. Modelling corticothalamic feedback and the gating of the thalamus by the
1006 cerebral cortex. *J. Physiol. Paris* **94**, 391–410 (2000).
1007 52. Haroian, A. J., Massopust, L. C. & Young, P. A. Cerebellothalamic projections in the rat: an
1008 autoradiographic and degeneration study. *J. Comp. Neurol.* **197**, 217–236 (1981)
1009 doi:10.1002/cne.901970205.
1010 53. Faull, R. L. The cerebellofugal projections in the brachium conjunctivum of the rat. II. The
1011 ipsilateral and contralateral descending pathways. *J. Comp. Neurol.* **178**, 519–535 (1978)

1012 doi:10.1002/cne.901780307.

1013 54. Card, J. P., Enquist, L. W. & Moore, R. Y. Neuroinvasiveness of pseudorabies virus
1014 injected intracerebrally is dependent on viral concentration and terminal field density. *J.*
1015 *Comp. Neurol.* **407**, 438–452 (1999) doi:3.0.co;2-2">10.1002/(sici)1096-
1016 9861(19990510)407:3<438::aid-cne11>3.0.co;2-2.

1017 55. Schmahmann, J. D. & Sherman, J. C. The cerebellar cognitive affective syndrome. *Brain*
1018 **121**, 561–579 (1998) doi:10.1093/brain/121.4.561.

1019 56. Apps, R. & Hawkes, R. Cerebellar cortical organization: a one-map hypothesis. *Nat. Rev.*
1020 *Neurosci.* **10**, 670–681 (2009) doi:10.1038/nrn2698.

1021 57. Wojaczynski, G. J., Engel, E. A., Steren, K. E., Enquist, L. W. & Patrick Card, J. The
1022 neuroinvasive profiles of H129 (herpes simplex virus type 1) recombinants with putative
1023 anterograde-only transneuronal spread properties. *Brain Struct. Funct.* **220**, 1395–1420
1024 (2015) doi:10.1007/s00429-014-0733-9.

1025 58. Smith, B. N. *et al.* Pseudorabies virus expressing enhanced green fluorescent protein: A
1026 tool for in vitro electrophysiological analysis of transsynaptically labeled neurons in
1027 identified central nervous system circuits. *Proc. Natl. Acad. Sci. U. S. A.* **97**, 9264–9269
1028 (2000) doi:10.1073/pnas.97.16.9264.

1029 59. Legg, C. R., Mercier, B. & Glickstein, M. Corticopontine projection in the rat: the distribution
1030 of labelled cortical cells after large injections of horseradish peroxidase in the pontine
1031 nuclei. *J. Comp. Neurol.* **286**, 427–441 (1989) doi:10.1002/cne.902860403.

1032 60. Ray, M., Tang, R., Jiang, Z. & Rotello, V. M. Quantitative tracking of protein trafficking to
1033 the nucleus using cytosolic protein delivery by nanoparticle-stabilized nanocapsules.
1034 *Bioconjug. Chem.* **26**, 1004–1007 (2015) doi:10.1021/acs.bioconjchem.5b00141.

1035 61. Conte, W. L., Kamishina, H. & Reep, R. L. Multiple neuroanatomical tract-tracing using
1036 fluorescent Alexa Fluor conjugates of cholera toxin subunit B in rats. *Nat. Protoc.* **4**, 1157–
1037 1166 (2009) doi:10.1038/nprot.2009.93.

1038 62. Callaway, E. M. Transneuronal circuit tracing with neurotropic viruses. *Curr. Opin.*
1039 *Neurobiol.* **18**, 617–623 (2008) doi:10.1016/j.conb.2009.03.007.
1040 63. Granstedt, A. E., Bosse, J. B., Thiberge, S. Y. & Enquist, L. W. In vivo imaging of
1041 alphaherpesvirus infection reveals synchronized activity dependent on axonal sorting of
1042 viral proteins. *Proc. Natl. Acad. Sci. U. S. A.* **110**, E3516–25 (2013)
1043 doi:10.1073/pnas.1311062110.
1044 64. Miranda-Saksena, M., Denes, C. E., Diefenbach, R. J. & Cunningham, A. L. Infection and
1045 Transport of Herpes Simplex Virus Type 1 in Neurons: Role of the Cytoskeleton. *Viruses*
1046 **10**, (2018) doi:10.3390/v10020092.
1047 65. Bria, A. & Iannello, G. TeraStitcher - a tool for fast automatic 3D-stitching of teravoxel-sized
1048 microscopy images. *BMC Bioinformatics* **13**, 316 (2012) doi:10.1186/1471-2105-13-316.
1049 66. Renier, N. *et al.* iDISCO: a simple, rapid method to immunolabel large tissue samples for
1050 volume imaging. *Cell* **159**, 896–910 (2014) doi:10.1016/j.cell.2014.10.010.
1051 67. Shamonin, D. P. *et al.* Fast parallel image registration on CPU and GPU for diagnostic
1052 classification of Alzheimer's disease. *Front. Neuroinform.* **7**, 50 (2013)
1053 doi:10.3389/fninf.2013.00050.
1054 68. Klein, S., Staring, M., Murphy, K., Viergever, M. A. & Pluim, J. P. W. elastix: a toolbox for
1055 intensity-based medical image registration. *IEEE Trans. Med. Imaging* **29**, 196–205 (2010)
1056 doi:10.1109/TMI.2009.2035616.
1057 69. Klein, S. & Staring, M. Image registration. in *Elastix, the manual* 13–16 (2015).
1058 70. Yoo, A. B., Jette, M. A. & Grondona, M. SLURM: Simple Linux Utility for Resource
1059 Management. in *Job Scheduling Strategies for Parallel Processing* 44–60 (Springer Berlin
1060 Heidelberg, 2003). doi:10.1007/10968987_3.
1061 71. Allen Institute for Brain Science. Technical white paper informatics data processing for the
1062 allen developing mouse brain atlas. (2012).
1063 72. Schmid, B., Schindelin, J., Cardona, A., Longair, M. & Heisenberg, M. A high-level 3D

1064 visualization API for Java and ImageJ. *BMC Bioinformatics* **11**, 274 (2010)
1065 doi:10.1186/1471-2105-11-274.
1066 73. Sergejeva, M. *et al.* Anatomical landmarks for registration of experimental image data to
1067 volumetric rodent brain atlasing templates. *J. Neurosci. Methods* **240**, 161–169 (2015)
1068 doi:10.1016/j.jneumeth.2014.11.005.
1069 74. Seabold, S. & Perktold, J. Statsmodels: Econometric and statistical modeling with python.
1070 in *Proceedings of the 9th Python in Science Conference* vol. 57 61 (Scipy, 2010).
1071 75. Roosendaal, T. & Selleri, S. *The Official Blender 2.3 guide: free 3D creation suite for*
1072 *modeling, animation, and rendering*. vol. 3 (No Starch Press San Francisco, CA, 2004).
1073 76. Jones, E., Oliphant, T. & Peterson, P. {SciPy}: Open source scientific tools for {Python}.
1074 (2001--).
1075 77. Chen, S., Yang, M., Miselis, R. R. & Aston-Jones, G. Characterization of transsynaptic
1076 tracing with central application of pseudorabies virus. *Brain Res.* **838**, 171–183 (1999).
1077 78. Aston-Jones, G. & Card, J. P. Use of pseudorabies virus to delineate multisynaptic circuits
1078 in brain: opportunities and limitations. *J. Neurosci. Methods* **103**, 51–61 (2000).
1079 79. van der Walt, S. *et al.* scikit-image: image processing in Python. *PeerJ* **2**, e453 (2014)
1080 doi:10.7717/peerj.453.
1081 80. Lee, K., Zung, J., Li, P., Jain, V. & Sebastian Seung, H. Superhuman Accuracy on the
1082 SNEMI3D Connectomics Challenge. *arXiv [cs.CV]* (2017).
1083 81. Gornet, J. *et al.* Reconstructing neuronal anatomy from whole-brain images. in (2019).
1084 82. Goutte, C. & Gaussier, E. A Probabilistic Interpretation of Precision, Recall and F-Score,
1085 with Implication for Evaluation. in *Advances in Information Retrieval* 345–359 (Springer
1086 Berlin Heidelberg, 2005). doi:10.1007/978-3-540-31865-1_25.
1087 83. Martinez, M., Calvo-Torrent, A. & Herbert, J. Mapping brain response to social stress in
1088 rodents with c-fos expression: a review. *Stress* **5**, 3–13 (2002)
1089 doi:10.1080/102538902900012369.

1090 84. Barski, J. J., Dethleffsen, K. & Meyer, M. Cre recombinase expression in cerebellar
1091 Purkinje cells. *Genesis* **28**, 93–98 (2000).
1092 85. Kloth, A. D. *et al.* Cerebellar associative sensory learning defects in five mouse autism
1093 models. *Elife* **4**, e06085 (2015) doi:10.7554/eLife.06085.
1094 86. Oliphant, T. E. Guide to NumPy. (2006).
1095 87. McKinney, W. & Others. Data structures for statistical computing in python. in *Proceedings*
1096 *of the 9th Python in Science Conference* vol. 445 51–56 (Austin, TX, 2010).
1097 88. Hunter, J. D. Matplotlib: A 2D Graphics Environment. *Comput. Sci. Eng.* **9**, 90–95 (2007)
1098 doi:10.1109/MCSE.2007.55.
1099 89. Waskom, M. *et al. seaborn: v0.5.0 (November 2014)*. (2014). doi:10.5281/zenodo.12710.
1100 90. Lowekamp, B. C., Chen, D. T., Ibáñez, L. & Blezek, D. The Design of SimpleITK. *Front.*
1101 *Neuroinform.* **7**, 45 (2013) doi:10.3389/fninf.2013.00045.
1102 91. Pedregosa, F. *et al.* Scikit-learn: Machine Learning in Python. *J. Mach. Learn. Res.* **12**,
1103 2825–2830 (2011).
1104 92. van Groen, T., Kadish, I. & Michael Wyss, J. Role of the anterodorsal and anteroventral
1105 nuclei of the thalamus in spatial memory in the rat. *Behav. Brain Res.* **132**, 19–28 (2002).
1106 93. Wang, C. C. & Shyu, B. C. Differential projections from the mediodorsal and centrolateral
1107 thalamic nuclei to the frontal cortex in rats. *Brain Res.* **995**, 226–235 (2004)
1108 doi:10.1016/j.brainres.2003.10.006.
1109 94. Bezdudnaya, T. & Keller, A. Laterodorsal nucleus of the thalamus: A processor of
1110 somatosensory inputs. *J. Comp. Neurol.* **507**, 1979–1989 (2008) doi:10.1002/cne.21664.
1111 95. Allen, A. E., Procyk, C. A., Howarth, M., Walmsley, L. & Brown, T. M. Visual input to the
1112 mouse lateral posterior and posterior thalamic nuclei: photoreceptive origins and retinotopic
1113 order. *J. Physiol.* **594**, 1911–1929 (2016) doi:10.1113/JP271707.
1114 96. Matsumoto, M. & Hikosaka, O. Representation of negative motivational value in the primate
1115 lateral habenula. *Nat. Neurosci.* **12**, 77–84 (2009) doi:10.1038/nn.2233.

1116 97. Lee, H. W., Yang, S. H., Kim, J. Y. & Kim, H. The Role of the Medial Habenula Cholinergic
1117 System in Addiction and Emotion-Associated Behaviors. *Front. Psychiatry* **10**, 100 (2019)
1118 doi:10.3389/fpsyt.2019.00100.
1119 98. Brown, H. D., Baker, P. M. & Ragozzino, M. E. The parafascicular thalamic nucleus
1120 concomitantly influences behavioral flexibility and dorsomedial striatal acetylcholine output
1121 in rats. *J. Neurosci.* **30**, 14390–14398 (2010) doi:10.1523/JNEUROSCI.2167-10.2010.
1122 99. Kirouac, G. J. Placing the paraventricular nucleus of the thalamus within the brain circuits
1123 that control behavior. *Neurosci. Biobehav. Rev.* **56**, 315–329 (2015)
1124 doi:10.1016/j.neubiorev.2015.08.005.
1125 100. Gauriau, C. & Bernard, J.-F. Posterior triangular thalamic neurons convey nociceptive
1126 messages to the secondary somatosensory and insular cortices in the rat. *J. Neurosci.* **24**,
1127 752–761 (2004) doi:10.1523/JNEUROSCI.3272-03.2004.
1128 101. Casas-Torremocha, D., Clascá, F. & Núñez, Á. Posterior Thalamic Nucleus Modulation of
1129 Tactile Stimuli Processing in Rat Motor and Primary Somatosensory Cortices. *Front. Neural*
1130 *Circuits* **11**, 69 (2017) doi:10.3389/fncir.2017.00069.
1131 102. Lam, Y.-W. & Sherman, S. M. Functional organization of the thalamic input to the thalamic
1132 reticular nucleus. *J. Neurosci.* **31**, 6791–6799 (2011) doi:10.1523/JNEUROSCI.3073-
1133 10.2011.
1134 103. Dolleman-van der Weel, M. J. *et al.* The nucleus reuniens of the thalamus sits at the nexus
1135 of a hippocampus and medial prefrontal cortex circuit enabling memory and behavior.
1136 *Learn. Mem.* **26**, 191–205 (2019) doi:10.1101/lm.048389.118.
1137 104. Tham, W. W. P., Stevenson, R. J. & Miller, L. A. The functional role of the medio dorsal
1138 thalamic nucleus in olfaction. *Brain Res. Rev.* **62**, 109–126 (2009)
1139 doi:10.1016/j.brainresrev.2009.09.007.
1140 105. Jankowski, M. M. *et al.* The anterior thalamus provides a subcortical circuit supporting
1141 memory and spatial navigation. *Front. Syst. Neurosci.* **7**, 45 (2013)

1142 doi:10.3389/fnsys.2013.00045.
1143 106. Starr, M. S. & Summerhayes, M. Role of the ventromedial nucleus of the thalamus in motor
1144 behaviour--II. Effects of lesions. *Neuroscience* **10**, 1171–1183 (1983).
1145 107. Vertes, R. P., Linley, S. B., Groenewegen, H. J. & Witter, M. P. Chapter 16 - Thalamus. in
1146 *The Rat Nervous System (Fourth Edition)* (ed. Paxinos, G.) 335–390 (Academic Press,
1147 2015). doi:10.1016/B978-0-12-374245-2.00016-4.
1148 108. Harrington, M. E. The ventral lateral geniculate nucleus and the intergeniculate leaflet:
1149 interrelated structures in the visual and circadian systems. *Neurosci. Biobehav. Rev.* **21**,
1150 705–727 (1997).
1151 109. Halassa, M. M. & Kastner, S. Thalamic functions in distributed cognitive control. *Nat.*
1152 *Neurosci.* **20**, 1669–1679 (2017) doi:10.1038/s41593-017-0020-1.
1153 110. Buckner, R. L. & DiNicola, L. M. The brain's default network: updated anatomy, physiology
1154 and evolving insights. *Nat. Rev. Neurosci.* **20**, 593–608 (2019) doi:10.1038/s41583-019-
1155 0212-7.

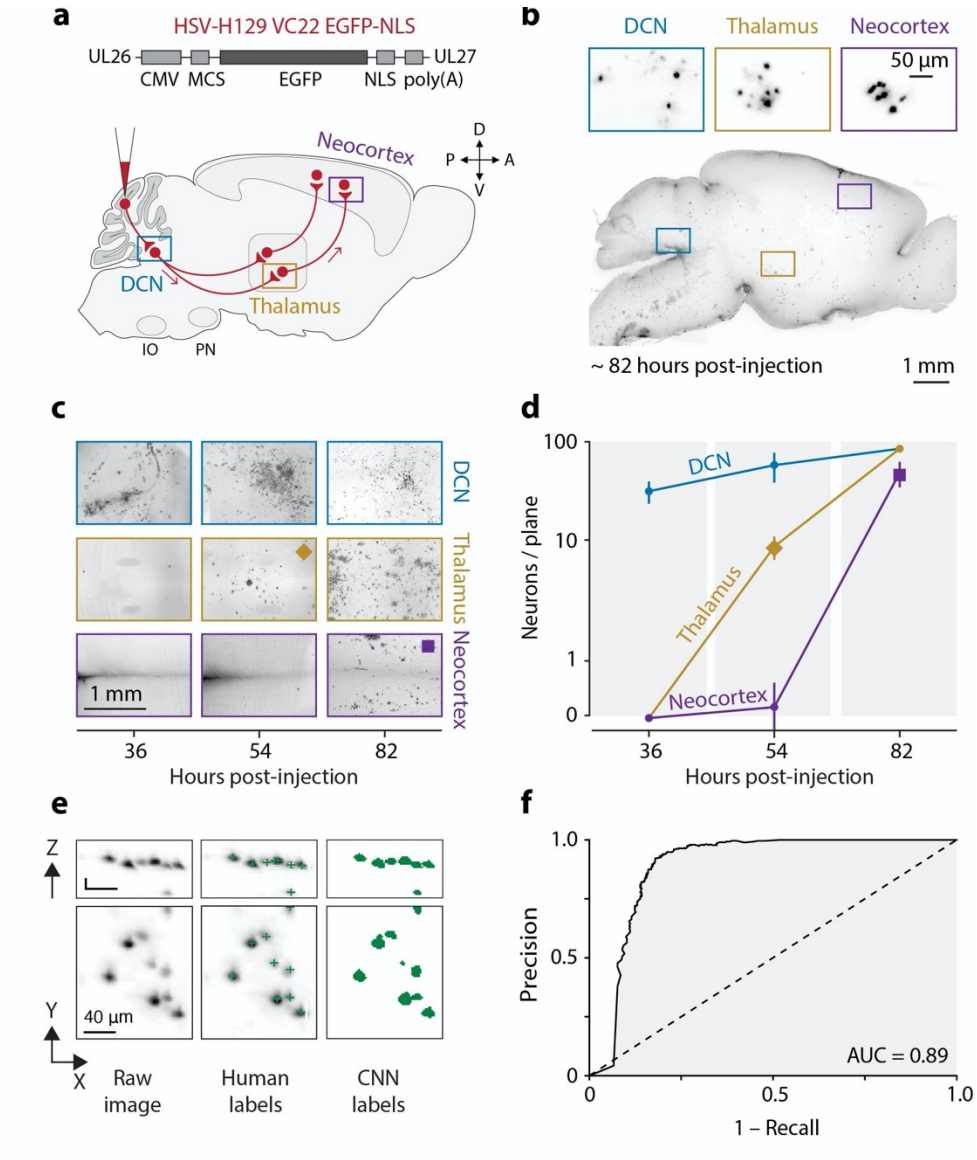

Figure 1. Large-scale transsynaptic tracing with tissue clearing and light-sheet microscopy. (a) *Top,* H129-VC22, a recombinant HSV-H129 virus that expresses a nuclear location signal tagged to an enhanced green fluorescent protein (EGFP). *Bottom,* experimental design to transsynaptically trace pathways from cerebellar cortex to thalamus and neocortex. (b) Example images of an iDISCO+ cleared brain ~82 hours post-injection. 158 µm maximum intensity projection. (c) Time course of infection. Images show horizontal maximum intensity projections of iDISCO+ cleared brains in the deep cerebellar nuclei (3.0 mm dorsal of bregma), thalamus (3.0 mm dorsal), and neocortex (0.7 mm dorsal). Dorsoventral depth of projection: 300 µm for deep cerebellar nuclei and thalamus, 150 µm for neocortex. (d) Quantification of viral spread. Cell counts from five planes from each brain region are shown. (e) Training data for convolutional neural network (CNN). *Left,* Representative images of raw input data. *Middle,* human-annotated cell centers (green overlay) for training the network. *Right,* segmented labels (green) used as training input. (f) Receiver operating characteristic curve for the trained neural net. The diagonal line indicates chance performance.

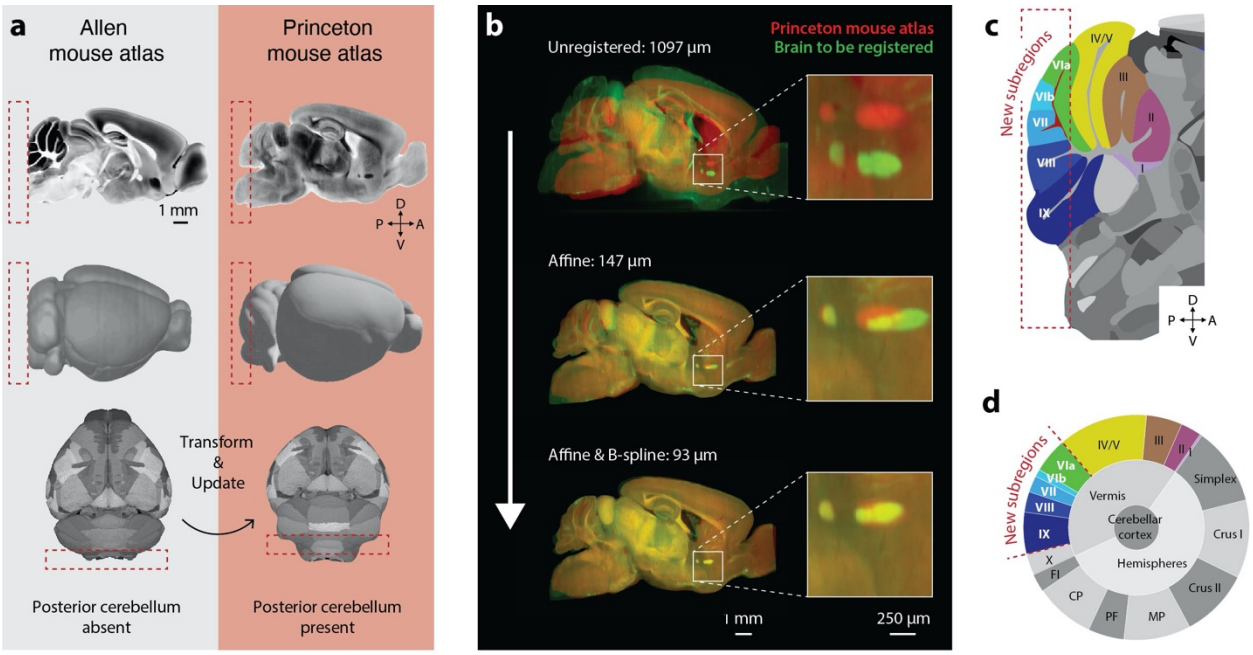

Figure 2. The Princeton Mouse Brain Atlas for light-sheet volume registration. (a) Sagittal views demonstrate differences between Allen Brain Atlas (ABA, left) and the Princeton Mouse Brain Atlas (PMA, right). The red dotted box indicates the caudal limit of the ABA. To map between PMA and ABA space, ABA annotations were transformed into PMA space. (b) Registration of whole-brain light-sheet volumes to the PMA. Light-sheet volume of an individual brain (green) overlaid with PMA (red) at different stages of registration. Median discrepancy is shown for each stage of alignment. (c) PMA cerebellar annotations. The red dotted box indicates newly annotated areas. (d) PMA cerebellar hierarchy depicting structure ontology and shows relative substructure size contributions. Abbreviations: PM, paramedian lobule; PF, paraflocculi; CP, copula pyramidis; Fl, flocculus.

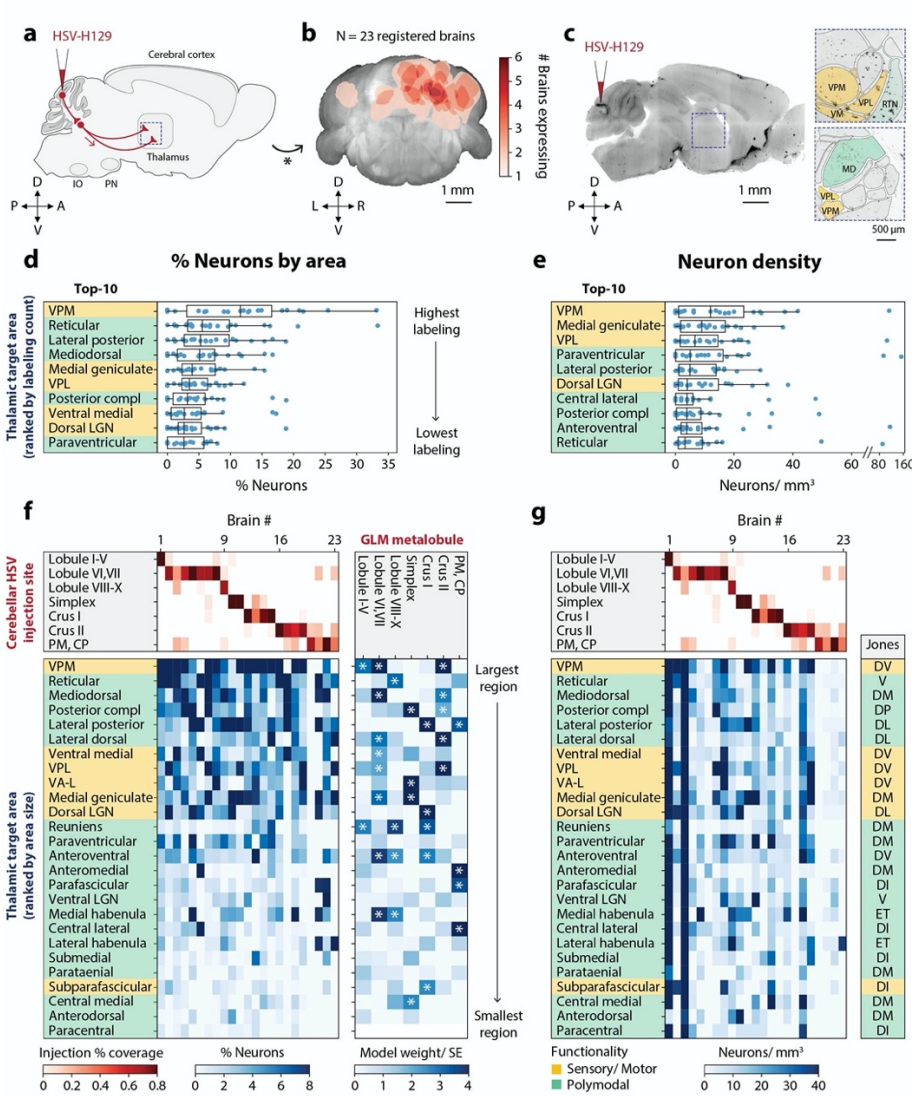

Figure 3. Cerebellar paths to thalamus. (a) Disynaptic path from the cerebellar cortex to thalamus traced using H129-VC22. (b) Coverage of cerebellum by thalamic timepoint injections. Coronal projections show the number of injections covering each location. (c) Example sagittal image of labeling ~54 hours post-injection, with outlines defining key thalamic nuclei. 150 µm maximum intensity projection. (d) Percentage fraction of neurons detected in each thalamic area. Each point represents one cerebellar injection site. Percentage fraction was calculated by dividing the number of neurons detected by the total number of neurons detected across all thalamus. The top 10 thalamic areas are shown. (e) Density of neurons in each thalamic area across all cerebellar injection sites. Top 10 areas are shown. (f) *Left*, fraction of neurons across all injection sites. Injection coverage fractions (red) and fraction of neurons (blue) are represented. One column represents one injection site. *Right*, a generalized linear model showing the influence of each cerebellar region on thalamic expression. The heatmap (blue) represents the coefficient divided by the standard error. Significant coefficients are marked with asterisks. (g) *Left*, density of neurons in each thalamic area across all cerebellar injection sites. *Right*, grouping according to[22]. For boxplots, whiskers are 1.5 times the interquartile range. Abbreviations: VPM, ventral posteromedial; VA-L, ventral anterior-lateral; VPL, ventral posterolateral; LGN, lateral geniculate nucleus.

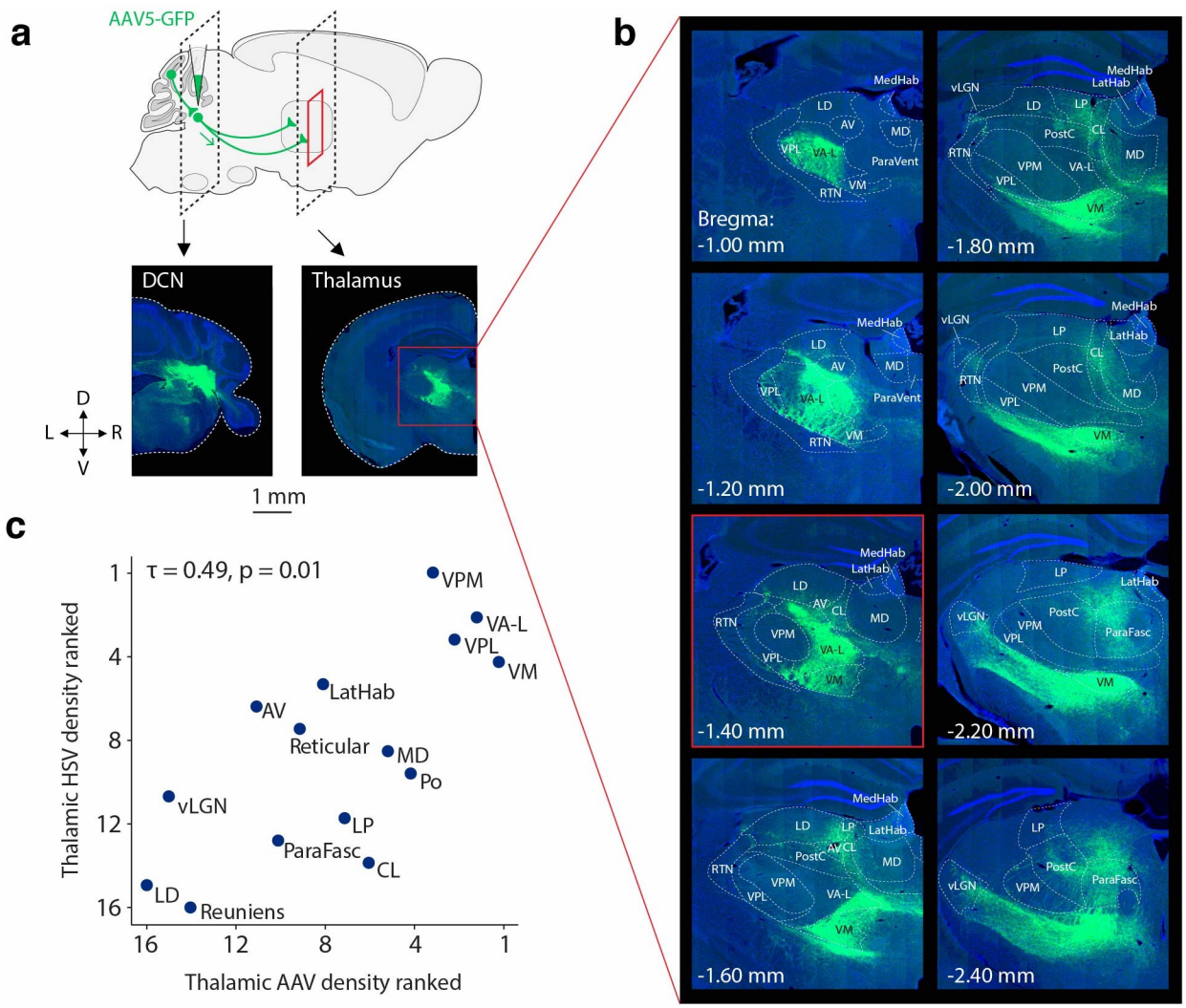

Figure 4. Cerebellothalamic AAV-identified axonal projections correspond with transsynaptic viral tracing. (a) Deep cerebellar nuclei were injected with AAV. Brains were coronally sectioned to identify cerebellothalamic axonal projection density. (b) Coronal sections after a deep cerebellar nuclear injection primarily targeting the dentate nucleus. Manually drawn Paxinos coronal overlays are shown. Bregma -1.40 mm corresponds to A. (c) Cerebellothalamic axons identified by AAV injections align with transsynaptic tracing. Kendall correlation (τ=0.49, p=0.01) of rank order density of HSV-labeled thalamic neurons after cerebellar cortical injection versus cerebellothalamic axonal projection density. Abbreviations: VPM, ventral posteromedial; VA-L, ventral anterior-lateral; VPL, ventral posterolateral; VM, ventral medial; LatHab, lateral habenula; AV, anteroventral; MD, mediodorsal; Po, posterior complex; LP, lateral posterior; CL, central lateral; ParaFasc, parafascicular; LD, lateral dorsal, vLGN, ventral lateral geniculate nucleus.

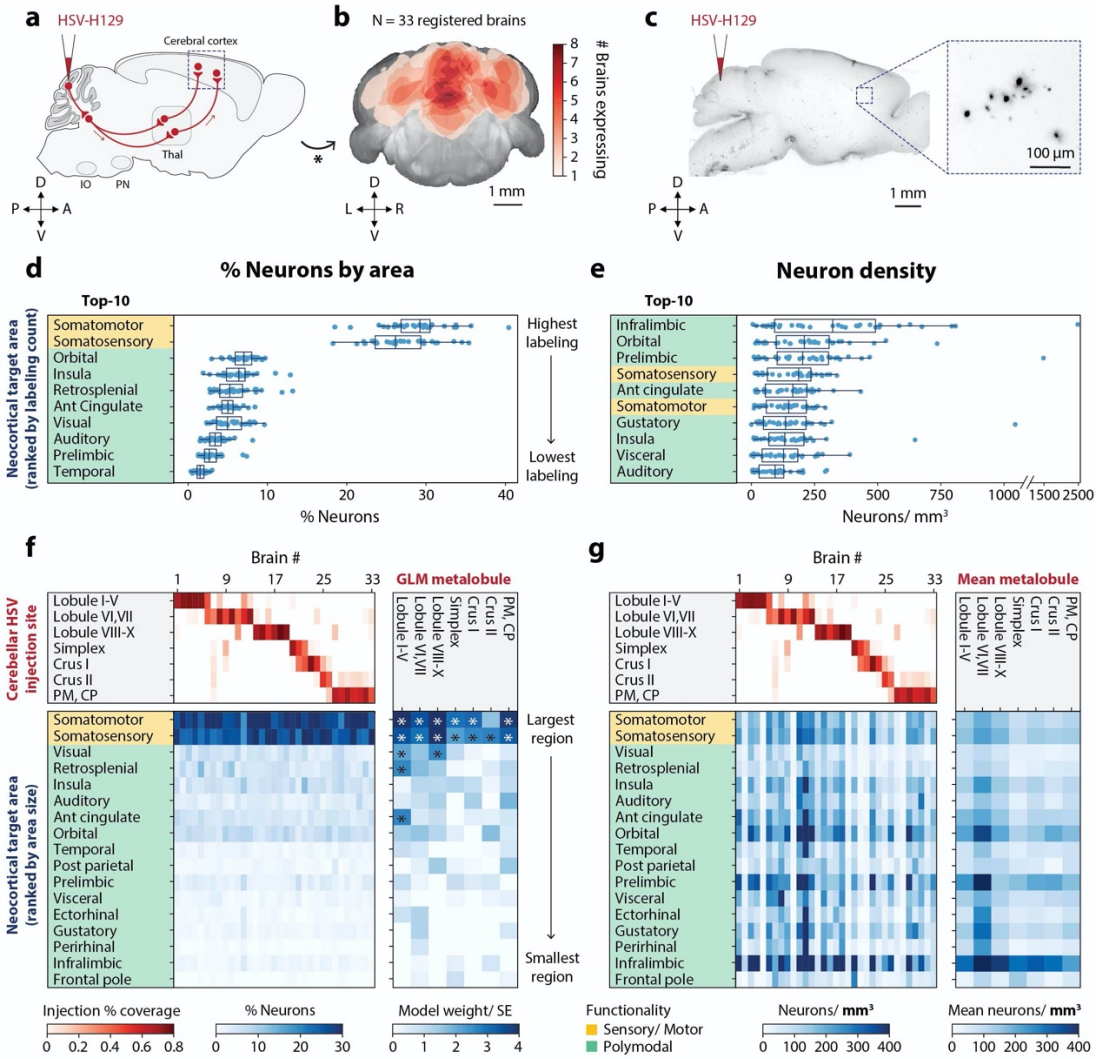

Figure 5. Cerebellar paths to neocortex. (a) The trisynaptic path from the cerebellar cortex to the neocortex traced using H129-VC22. (b) Coverage of cerebellum by neocortical timepoint injections. Coronal projections show the number of injections covering each cerebellar location. (c) Example sagittal image of labeling ~80 hours post-injection. 158 µm maximum intensity projection. (d) Fraction of neurons detected in each neocortical area across all cerebellar injection sites. The fraction was calculated by dividing the number of neurons detected in each area by the total number of neurons detected across all neocortex. The top 10 areas are shown. (e) Density of neurons in each neocortical area across all cerebellar injection sites. The top 10 neocortical areas with the densest labeling are shown. (f) *Left*, fraction of neurons in each neocortical area across all injection sites. Injection coverage fractions (red) and fraction of neurons (blue) are represented for each brain injected. Brains are ordered by primary injection site. *Right*, a generalized linear model showing the influence of each cerebellar region on neocortical expression. The heatmap (blue) represents the coefficient divided by the standard error. Significant coefficients are marked with asterisks. (g) *Left*, density of neurons in each neocortical area across all injections. *Right*, mean density of neurons. For boxplots, whiskers are 1.5 times the interquartile range. Abbreviations: Ant, anterior; CP, Copula pyramidis; PM, Paramedian; Post, posterior.

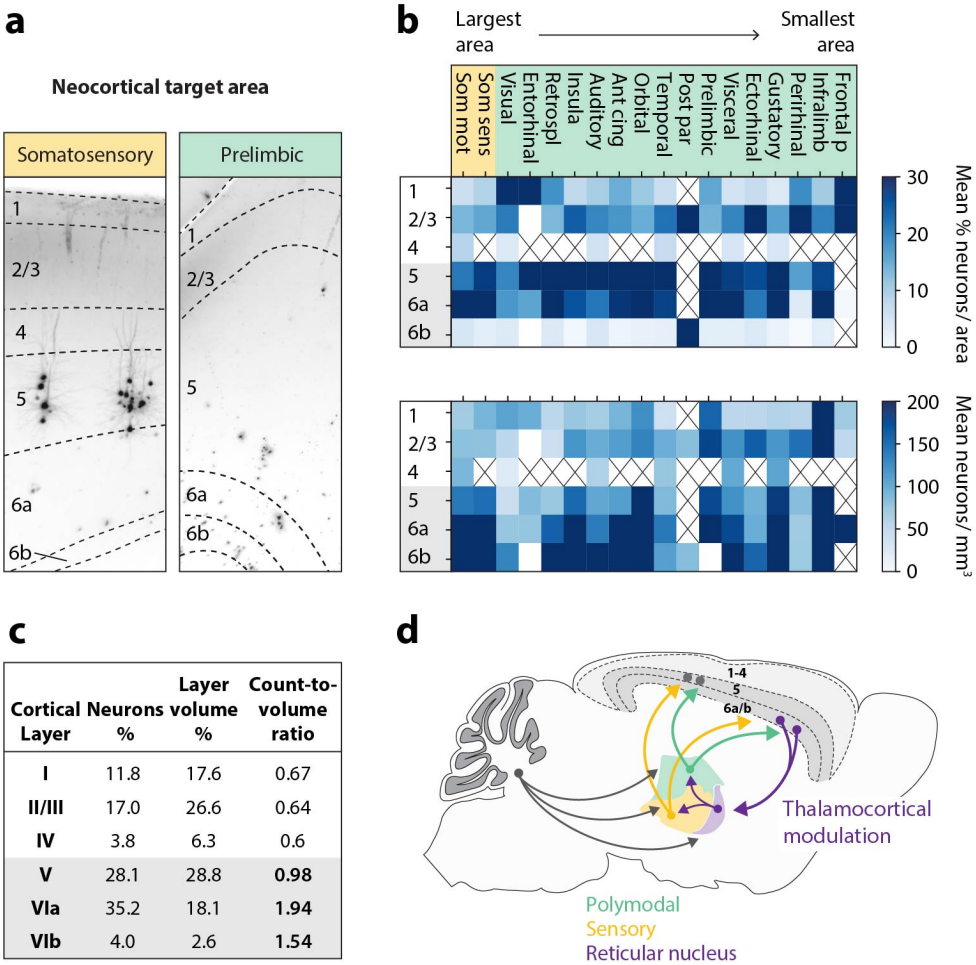

Cortical Layer	Neurons %	Layer volume %	Count-to-volume ratio
I	11.8	17.6	0.67
II/III	17.0	26.6	0.64
IV	3.8	6.3	0.6
V	28.1	28.8	**0.98**
VIa	35.2	18.1	**1.94**
VIb	4.0	2.6	**1.54**

Figure 6. Cerebellar projections to thalamocortical and deep-layer modulatory systems. (a) Example images of labeling in the neocortex ~80 hours post-injection, with outlines defining neocortical layers in each area. 75 μm maximum intensity projections. (b) Distribution of neocortical neurons in layers by neocortical area. *Top*, mean percentage of neurons normalized by area. *Bottom*, mean density of neurons. (c) Layer distribution of counts aggregated across all of neocortex. (d) Summary of cerebellar output connectivity to thalamus and neocortex demonstrated by transsynaptic tracing. Thalamic targets include sensory relay nuclei, polymodal association nuclei, and the reticular nucleus. Abbreviations: Som mot, somatomotor; Som sens, somatosensory; Retrospl, retrosplenial; Ant cing, anterior cingulate; Post par, posterior parietal; Infralimb, infralimbic; Frontal p, frontal pole.

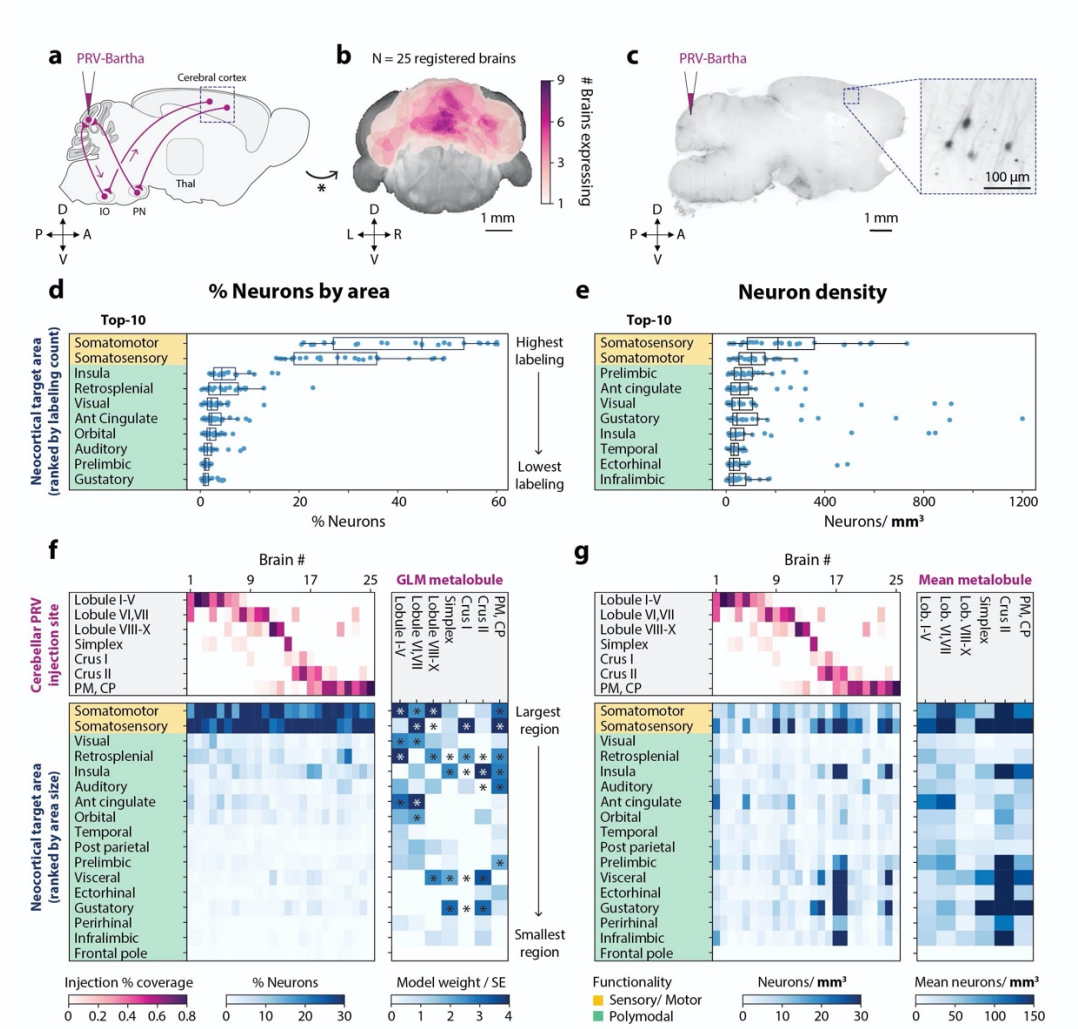

Figure 7. Descending projections to cerebellar cortex labeled using PRV-Bartha. (a) Schematic of the retrograde trisynaptic path from the cerebellar cortex to the neocortex traced using PRV-Bartha. (b) Coverage of cerebellum by neocortical timepoint injections. Coronal projections show the number of injections covering each cerebellar location. (c) Example sagittal image of typical labeling ~80 hours post-injection. 375 µm maximum intensity projection. (d) Fraction of neurons detected in each neocortical area across all injection sites. The percentage fraction was calculated by dividing the number of neurons detected in each area by the total number of neurons detected in neocortex. The top 10 neocortical areas with the most labeling are shown. (e) Density of neurons in each neocortical area across all cerebellar injection sites. The top 10 neocortical areas with the densest labeling are shown. (f) *Left*, fraction of neurons in each neocortical area across all injection sites. Injection coverage fractions (pink) and fraction of neurons (blue) are represented for each brain injected. *Right*, a generalized linear model showing the influence of each cerebellar region on neocortical expression. The heatmap (blue) represents the coefficient divided by the standard error. Significant coefficients are marked with asterisks. (g) *Left*, density of neurons in each neocortical area across all cerebellar injection sites. *Right*, mean density of neurons in each neocortical area grouped by primary injection site. For boxplots, whiskers are 1.5 times the interquartile range. Abbreviations: Ant, anterior; CP, Copula pyramidis; PM, Paramedian; Post, posterior.

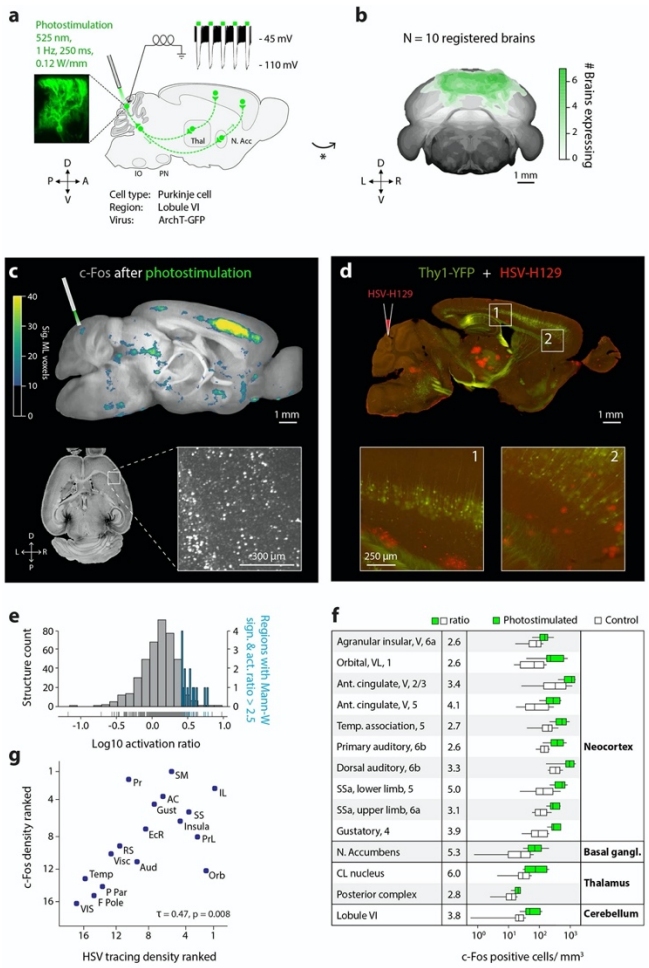

Figure 8. Cerebellar perturbation activates transsynaptically connected regions across the brain. (a) Experimental setup for photostimulating the inhibitory optogenetic protein ArchT-GFP through a cranial window over cerebellar lobule VI. *Top*, silencing of Purkinje cells as measured in brain-slice whole-cell recordings after photostimulation with 525 nm light. (b) Coverage of cerebellum by ArchT-GFP expression. Coronal projections show the number of injections covering each cerebellar location. (c) Neural activity identified by c-Fos immunostaining. *Top*, voxel-by-voxel regions of statistically significant c-Fos activation in Princeton Mouse Atlas (PMA) space (planes 320-360, 20 μm isotropic voxel size). *Bottom*, example horizontal image of typical c-Fos labeling after optogenetic perturbation. 132 μm maximum intensity projection. (d) Transsynaptic targets of lobule VI labeled using H129-VC22 (red) injected into Thy1-YFP (green) mice. Standard non-clearing histological imaging, 50 μm section, 80 hpi. (e) Activation ratios, defined by number of c-Fos neurons in photostimulated divided by control-group, for all brain regions. Regions were scored as responding (blue coloring) if they had activation ratios greater than 2.5 and $p<0.05$ by two-tailed Mann-Whitney test. (f) Distribution of c-Fos neurons for all responding regions. (g) Rank order of c-Fos density is positively correlated (Kendall's $\tau=+0.47$) with rank order from transsynaptic tracing. Abbreviations: AC, anterior cingulate; ant, anterior; Aud, auditory; C, caudal; D, dorsal; EcR, ectorhinal area; IL, infralimbic; Insula, agranular insula; F Pole, frontal pole; Gust, gustatory areas; n., nucleus; Orb, orbital area; P Par, posterior parietal; PR, perirhinal areas; PrL, prelimbic; RS, retrosplenial area; SC, superior colliculus; SM, somatomotor areas; SS, somatosensory areas; Temp, temporal; V, ventral; VIS, visual; Visc, visceral area.

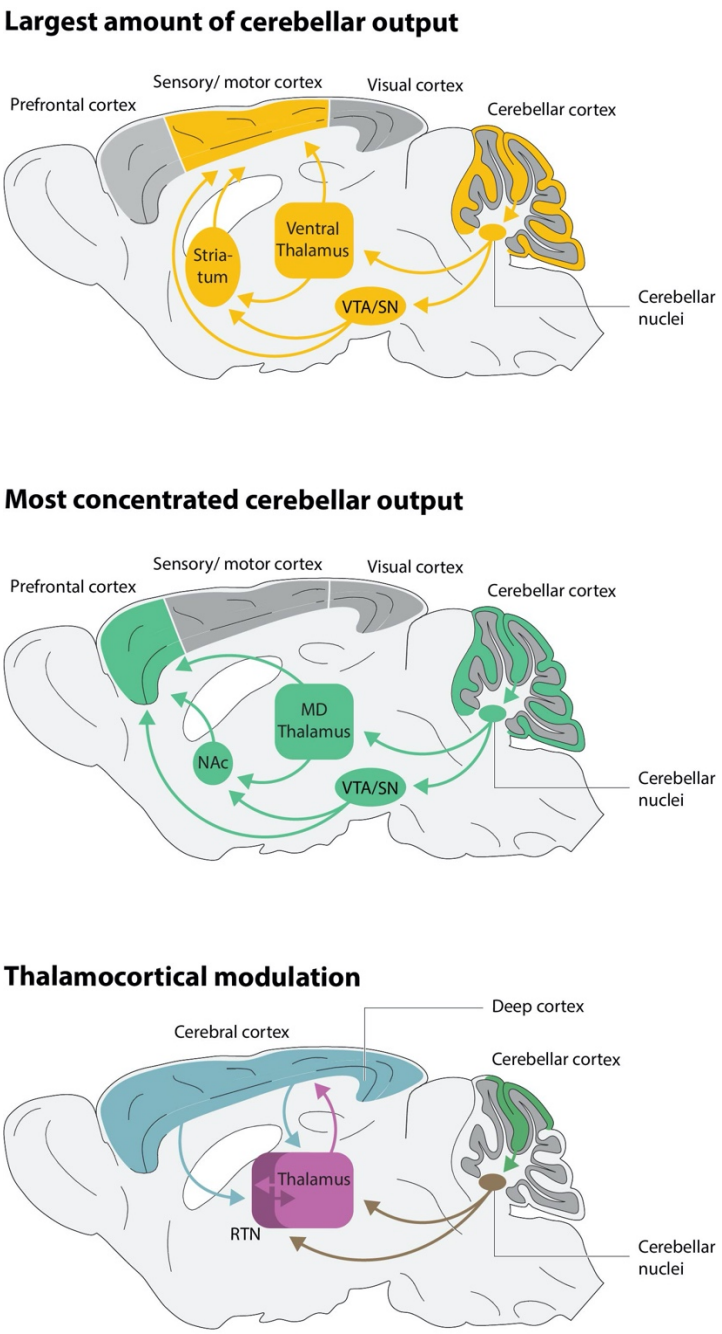

Figure 9. Parallel ascending cerebellar pathways for sensorimotor, associative, and regulatory function. *Top*, the most cerebellar projections in thalamus and neocortex are found in sensorimotor structures. *Middle*, the densest cerebellar projections are found in frontal neocortical structures. *Bottom*, the cerebellum projects to thalamocortical regions involved in sensory modulation, attentional selection [109], and control of processing [110].

CNN	Different brains	Different volumes	Number of cells	Human-CNN concordance	Human-human concordance
H129	8	44	3603	F1: 0.864 Precision: 0.912 Recall: 0.821	F1: 0.891 Precision: 0.947 Recall: 0.842 1091 cells annotated by both users
PRV	7	41	5119	F1: 0.873 Precision: 0.833 Recall: 0.926	F1: 0.886 Precision: 0.936 Recall: 0.841 1280 cells annotated by both users

1281 **Table 1.** Training datasets descriptions used to train cell detectors.

Thalamic Area	General function	Reference
Anteroventral	Spatial Memory	92
Central lateral	Emotional aspects of nociception	93
Lateral dorsal	Somatosensory processing	94
Lateral posterior	Visually-guided behavior	95
Lateral habenula	Reward Negative	96
Mediodorsal	Processing/integration of memory/cognition	23
Medial habenula	Emotion-associated behavior	97
Parafascicular	Reversal Learning	98
Paraventricular	Emotional arousal, +/- behavioral mediation	99
Posterior triangle	Nociception	100
Posterior complex	Adjusting response to unexpected sensory input	101
Reticular	Cortical-based modulation of thalamus	102
Reuniens	Hippocampal modulation	103
Submedial	Olfaction	104
VA-L	Memory/Spatial navigation & Motor	105
Ventral medial	Motor	106
VPL	Sensory Body	107
VPM	Sensory Face	107

Ventral LGN	Visuomotor response & Circadian rhythms	[108]

1282 **Table 2.** Thalamic target area function references. Abbreviations: VA-L, ventral anterior-lateral;

1283 VPL, ventral posterolateral; VPM, ventral posteromedial; LGN, lateral geniculate nucleus.

Target	Injection	Primary antibody	Secondary antibody
c-Fos	rAAV1-CAG-FLEX-ArchT-GFP	1:2000 Rabbit anti-c-Fos Synaptic Systems Cat. No. 226003	1:500 Donkey anti-Rabbit AlexaFluor 790 ThermoFisher A11374
Anterograde thalamic timepoint (53 hpi)	H129-VC22 ($2.7x10^4$ to $8.0x10^4$ PFUs)	1:350 Rabbit anti-HSV Dako B011402-2	1:250 Donkey anti-Rabbit AlexaFluor 647 ThermoFisher A31573
Anterograde neocortical timepoint (80 hpi)	H129-VC22 ($2.7x10^4$ to $8.0x10^4$ PFUs)	1:1750 Rabbit anti-HSV Dako B011402-2	1:500 Donkey anti-Rabbit AlexaFluor 647 ThermoFisher A31573
Retrograde neocortical timepoint (80 hpi)	PRV-Bartha 152 ($6.0x10^4$ PFUs)	1:500 Chicken anti-GFP Aves GFP-1020	1:300 Donkey anti-Chicken AlexaFluor 647 Jackson ImmunoResearch 703-606-155

1284 **Table 3.** Experimental injection and clearing protocols for transsynaptic and physiologic tracing

1285 from cerebellum. Abbreviations: hpi, hours post-injection.

Structure	Timepoint	Number of brains	Edge erosion	Ventricular erosion
Thalamus (H129)	55 hpi	23	60 μm	80 μm
Neocortex (H129)	80 hpi	33	60 μm	80 μm
Striatum (H129)	80 hpi	33	60 μm	80 μm
Hypothalamus (H129)	80 hpi	31	60 μm	160 μm
Neocortex (PRV)	80 hpi	25	60 μm	80 μm

1286 **Table 4.** Cohort details for each structure analyzed. Abbreviations: hpi, hours post-injection.

ClearMap parameter	Value
`removeBackgroundParameter_size`	(5,5)
`findExtendedMaximaParameter_size`	(5,5)
`findExtendedMaximaParameter_threshold`	0
`findIntensityParameter_size`	(3,3,3)
`detectCellShapeParameter_threshold`	105

1287 **Table 5.** ClearMap parameters used on whole-brain light-sheet volumes for detecting c-Fos

1288 positive neurons.

Target	Cerebellar injection site	Structure	Mean ± std. dev.
Anterograde thalamic timepoint (53 hpi)	All injections	Sensory-motor	2.5 ± 5.7
		Polymodal association	1.0 ± 0.7
	Vermis	Sensory-motor	1.6 ± 2.4
		Polymodal association	1.0 ± 0.6
	Hemisphere	Sensory-motor	3.5 ± 7.8
		Polymodal association	1.2 ± 0.9
Anterograde neocortical timepoint (80 hpi)	All injections	Frontal	1.2 ± 0.5
		Medial	1.2 ± 0.4
		Posterior	1.0 ± 0.4
	Vermis	Frontal	1.2 ± 0.5
		Medial	1.2 ± 0.5
		Posterior	1.0 ± 0.5
	Hemisphere	Frontal	1.3 ± 0.4
		Medial	1.2 ± 0.3
		Posterior	1.2 ± 0.3
Retrograde neocortical timepoint (80 hpi)	All injections	Frontal	1.4 ± 0.6
		Medial	3.2 ± 2.8
		Posterior	1.7 ± 1.5
	Vermis	Frontal	1.2 ± 0.3
		Medial	2.7 ± 3.1
		Posterior	1.3 ± 0.8
	Hemisphere	Frontal	1.6 ± 0.7

		Medial	3.9 ± 2.4
		Posterior	2.2 ± 1.8

1289 **Supplementary Table 1**. Contralateral-to-ipsilateral projection ratios for sub-regions in
1290 ascending and descending cerebellar pathways traced using H129-VC22 and PRV-Bartha.
1291 Front neocortical regions include infralimbic, prelimbic, anterior cingulate, orbital, frontal pole,
1292 gustatory, auditory, and visual cortex; medial regions include somatomotor and somatosensory
1293 cortex; posterior regions include retrosplenial, posterior parietal, temporal, perirhinal, and
1294 ectorhinal cortex.

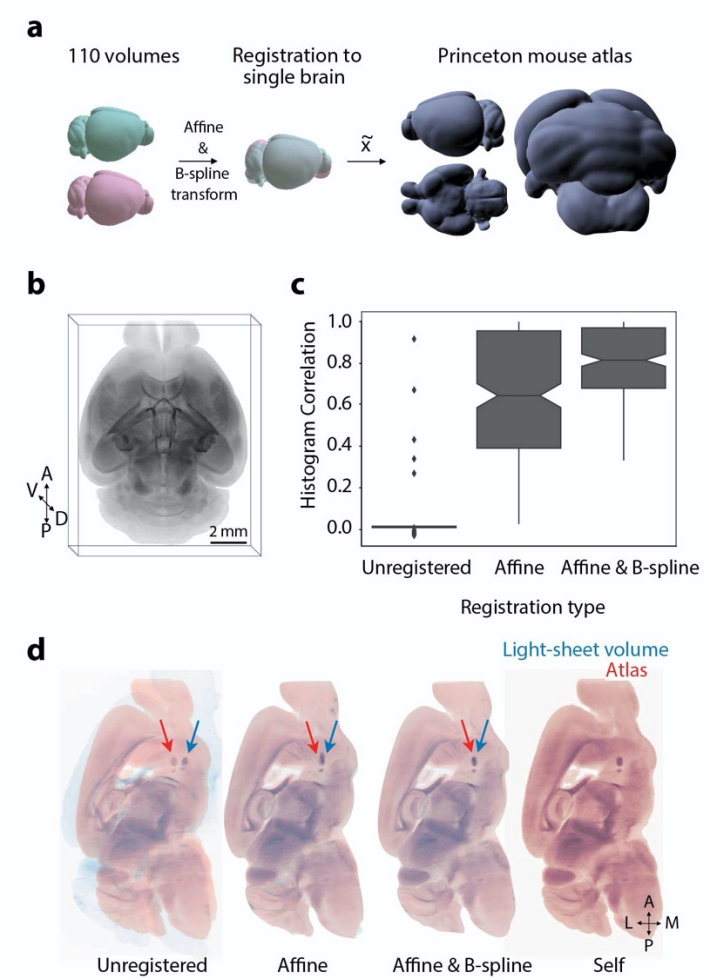

Supplementary Figure 1. The Princeton mouse atlas, a light-sheet volumetric atlas with a complete cerebellum. (a) Schematic depicting atlas generation. Mouse brains cleared using iDISCO+ (n=110) were imaged using a light-sheet microscope were resampled to 20 µm/voxel. A single volume was selected and the other brains registered to it. The median XYZ voxel was then used from the resulting metabrain. (b) Three-dimensional projection rendering ("3D project" function, ImageJ) of the light-sheet atlas. (c) Histogram correlations demonstrate human-independent improvement in volumetric alignment. Pearson's correlations (scipy.stats) were calculated using normalized histograms (bins=300) for unregistered (r=.005, p=.856, medians), affine (r=0.518, p=4.94 x 10^-22), and affine & B-spline (r=0.712, p=1.26 x 10^-47) registered volumes (n=224) with the PMA. (d) Color-blind friendly version demonstrating landmark alignment example.

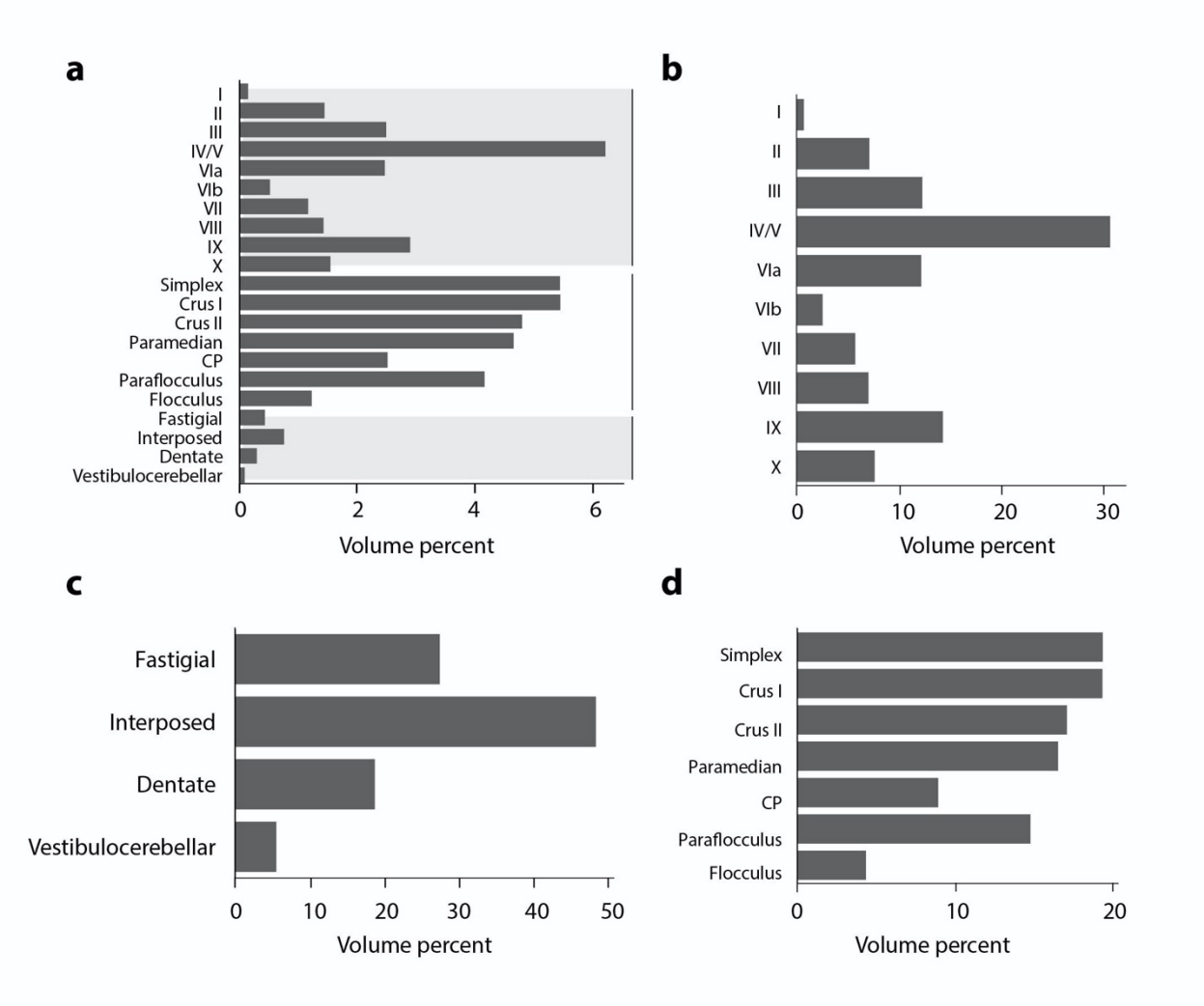

Supplementary Figure 2. Percent contributions of substructures to cerebellar volume in the PMA. (a) Cerebellar substructure percent volumes. Bar plot depicts volumes as percentage of gross cerebellar volumes in the PMA. Relative volume percentages of substructures in the vermis (b), deep cerebellar nuclei (c), and hemispheres (d) are also shown. Abbreviations: CP, copula pyramidis.

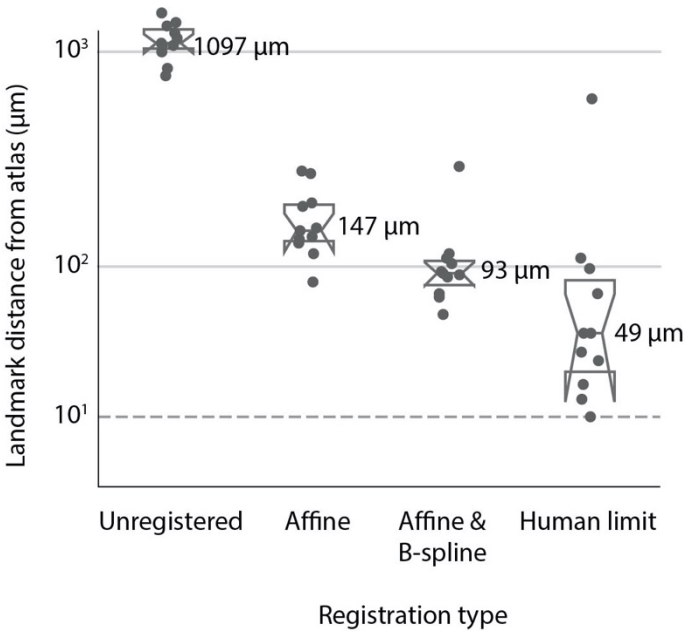

Supplementary Figure 3. Landmark euclidean distance quantification demonstrates registration performance. Users (n=11), blinded to each volume's condition, annotated a total of 69 complementary points, across four brains, in unregistered (two identical volumes, human precision), affine, affine & B-spline. Three-dimensional euclidean distances were determined. Points are median user performance per condition and numbers displayed are median distances across users. Dashed horizontal line depicts single voxel distance (20 μm).

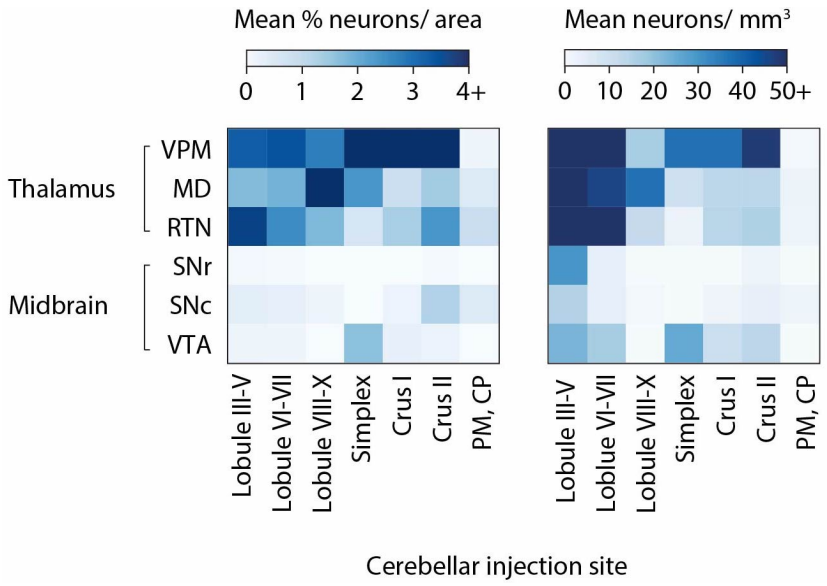

Supplementary Figure 4. Cerebellar paths to ventral tegmental area are weaker than thalamic projections. *Right*, mean percentage of total thalamic and midbrain neurons in each region grouped by primary injection site. *Left,* mean density of neurons in each region grouped by primary injection site. The top 3 most labeled thalamic regions and selected midbrain regions are shown.

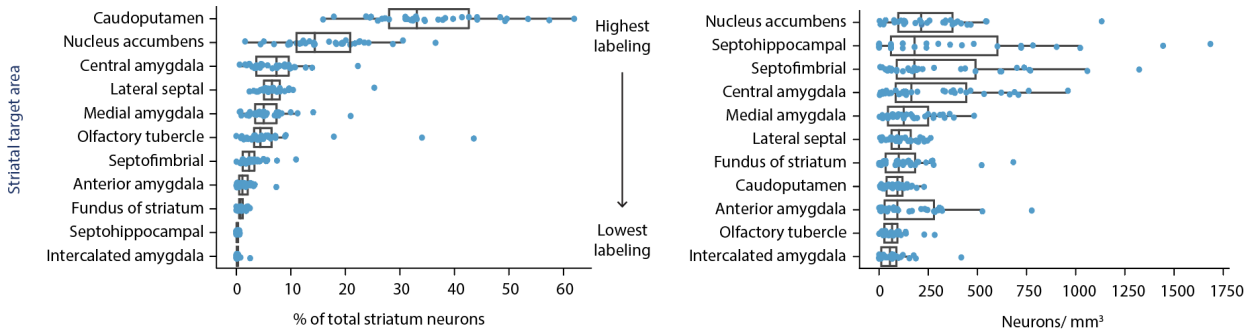

Supplementary Figure 5. Cerebellar projections to the contralateral striatum at the neocortical timepoint. Percent of total labeled striatal neurons (left) and neuron density (right) for each structure are shown. Median and quartiles 1 and 3 shown, whiskers are 1.5 times the interquartile range.

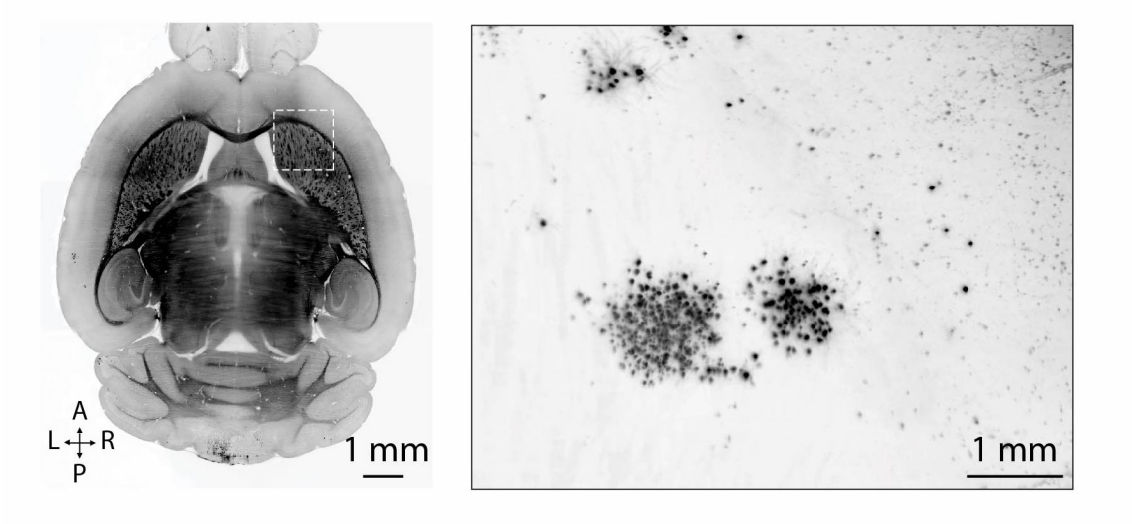

Supplementary Figure 6. The striatum receives cerebellar input in dense striosome-like clusters. Example viral labeling after a lobule VIII midline injection. 300 μm maximum intensity projection. Autofluorescent horizontal plane used for anatomical reference.

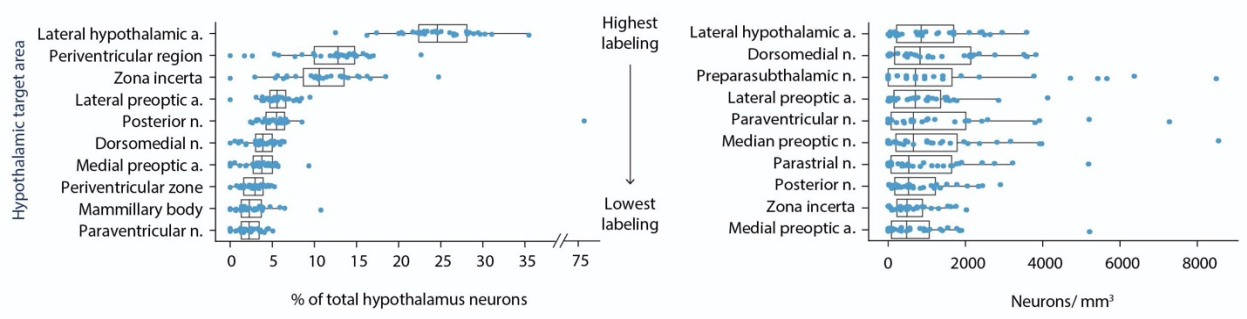

Supplementary Figure 7. Cerebellar output to bilateral hypothalamus. Percent of total labeled hypothalamic neurons (left) and neuron density (right) for each structure are shown. To minimize false positives, areas around ventricles were eroded by 160 μm removing some volume from the hypothalamic areas around ventral portions of the third ventricle. Median and quartiles 1 and 3 shown, whiskers are 1.5 times the interquartile range. Abbreviations: a., area; n., nucleus.

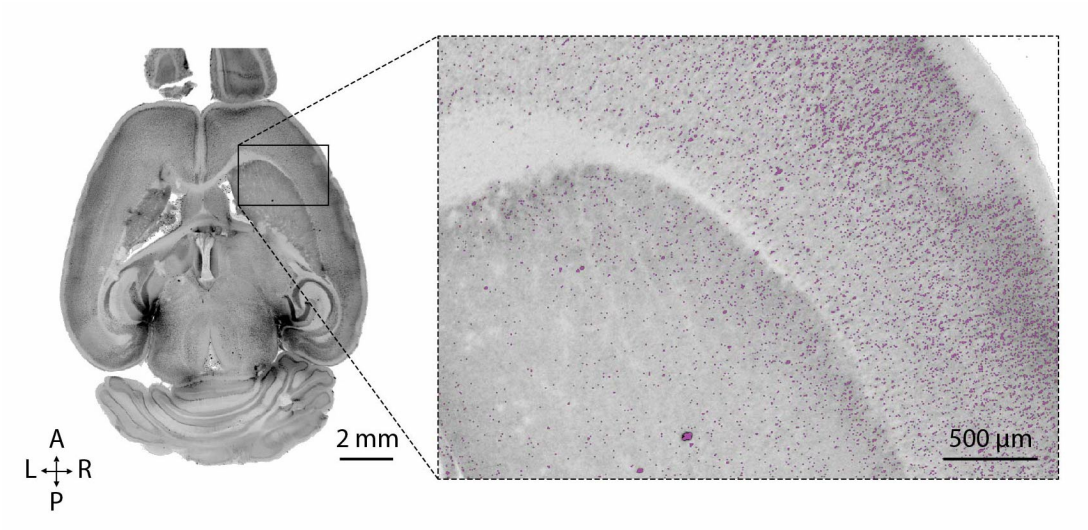

1335 **Supplementary Figure 8**. ClearMap automatically quantifies c-Fos expression. A horizontal
1336 image of a whole mouse brain with c-Fos antibody labeling (left) and overlay of c-Fos (gray) with
1337 c-Fos positive cells detected using ClearMap (purple) are shown. 132 µm maximum intensity
1338 projection.

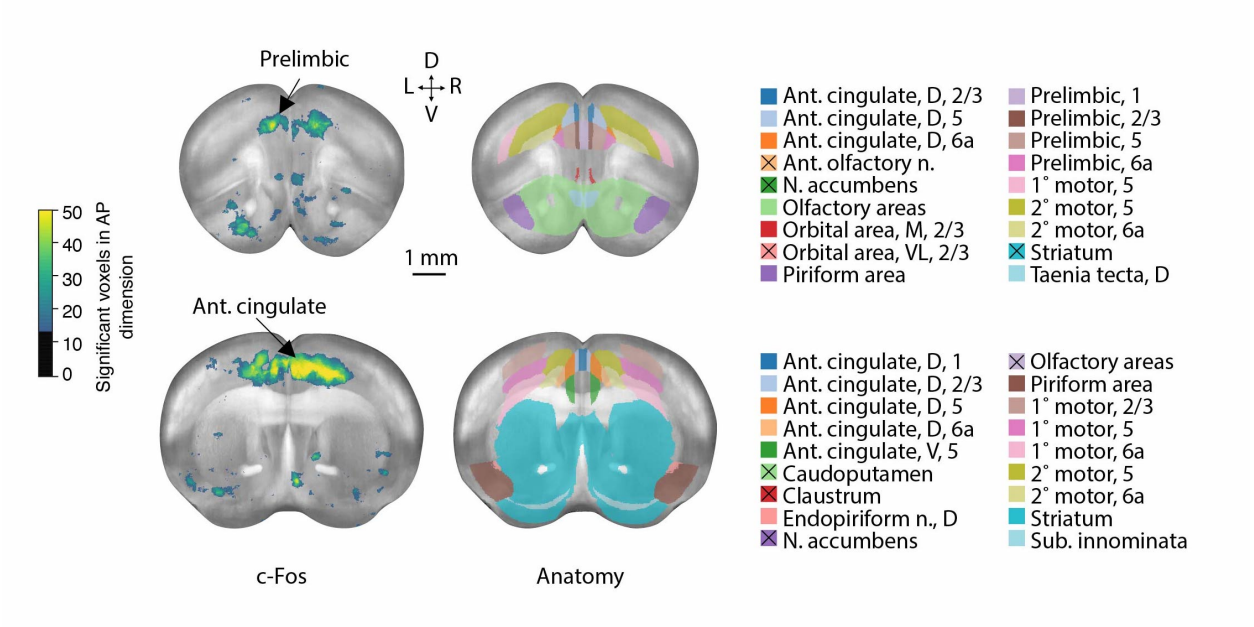

Supplementary Figure 9. Cortical areas show increased c-Fos cell counts after cerebellar optogenetic perturbation. Coronal maximum intensity projections (left) across 1 mm of tissue corresponding to Princeton mouse atlas planes 100-150 (top) and 150-200 (bottom) after 375 µm spherical voxelization. Complementary sections (right) with anatomical labels of 18 structures with the largest number of significant voxels. Structures with the largest AP span are shown when they overlap. Black X's in legend denote structures not shown due to overlap. Schematic in lower left of D shows coronal ranges. Abbreviations: 1˚, primary; 2˚, secondary; ant, anterior; AP, anteroposterior, D, dorsal; L, lateral, M, medial; n., nucleus; SS, somatosensory; sub, substania; V, ventral.

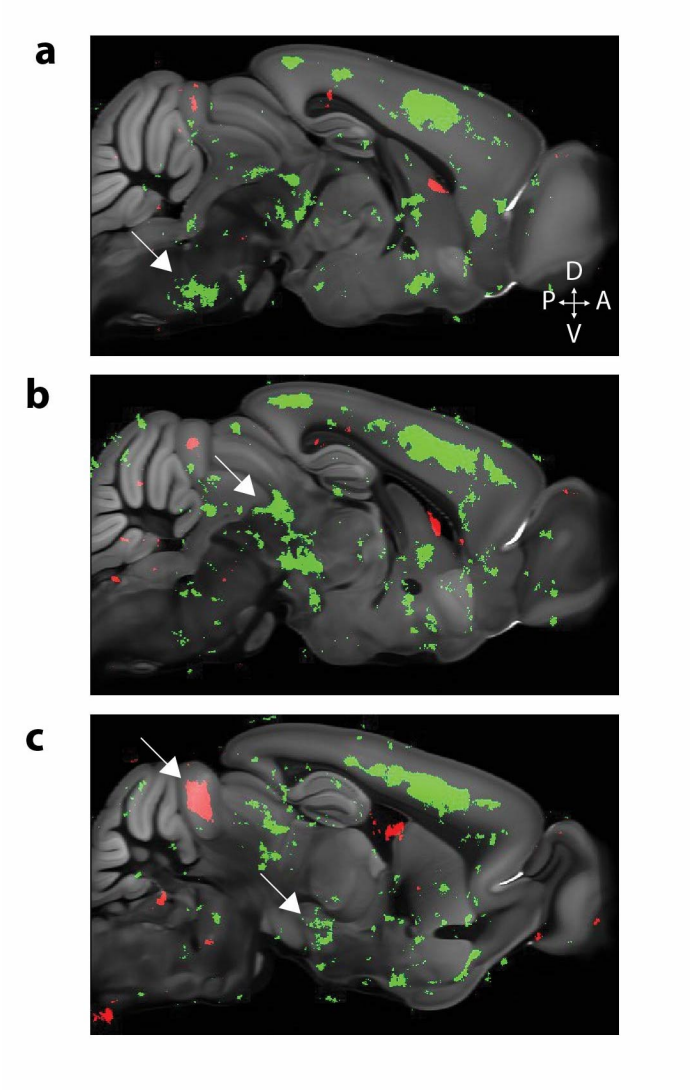

Supplementary Figure 10. c-Fos p-value maps comparing brain regions activated by cerebellar optogenetic perturbation (green) vs. controls (red) reveal patterns of activation in pontine nuclei (a), midbrain (b), and superior colliculi (upper arrow) and hypothalamus (lower arrow) (c). White arrows in each panel indicate named regions of interest. Significant voxels (green or red) are shown overlaid on the Allen Brain Atlas template brain.

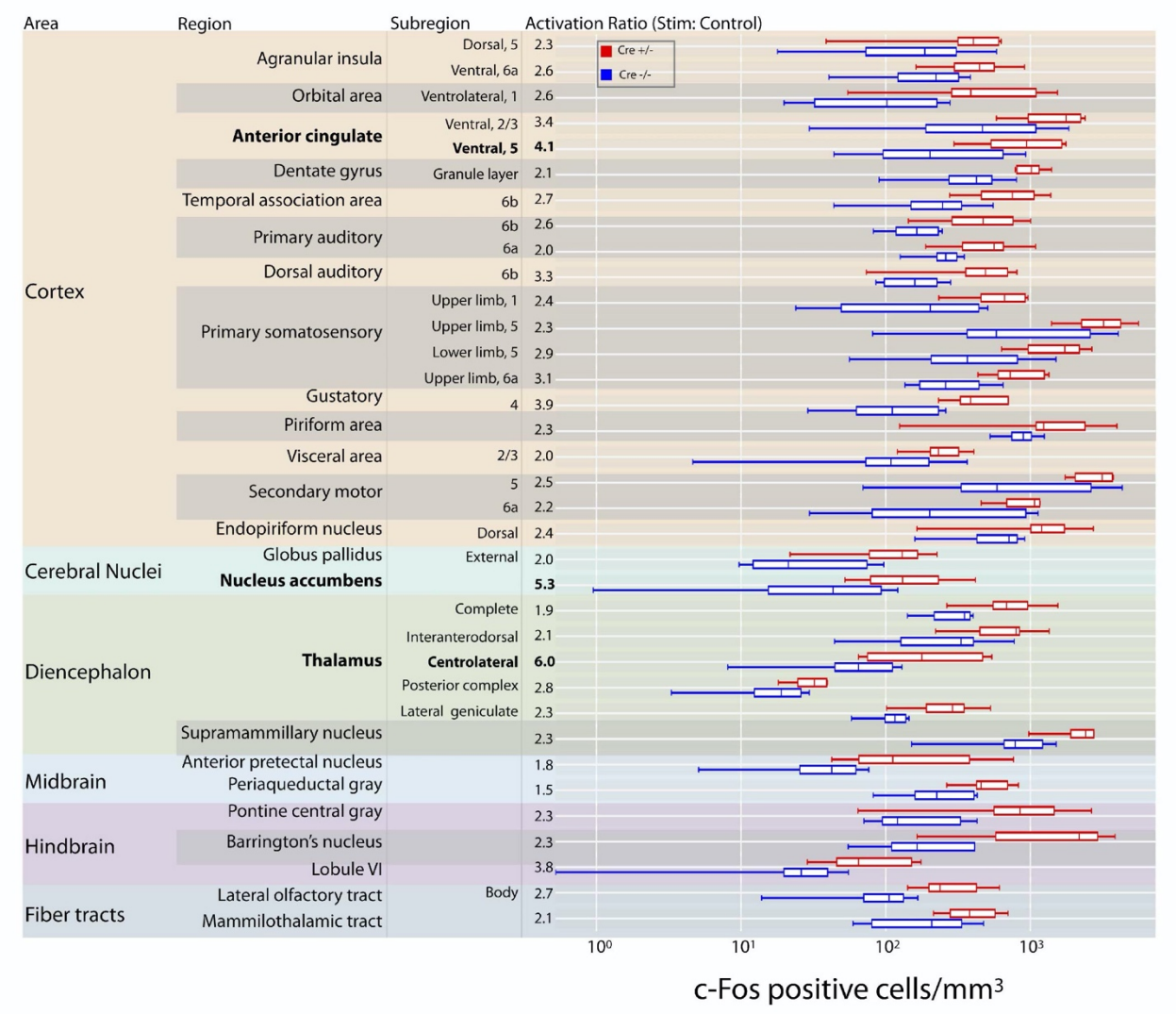

Supplementary Figure 11. A brain-wide nonmotor network traced from the cerebellum. Lobule VI Purkinje cell inhibition leads to strong activity increases in nonmotor areas including the anterior cingulate, nucleus accumbens and centrolateral nucleus of thalamus. Structures listed have a Mann-Whitney p-value < 0.05.

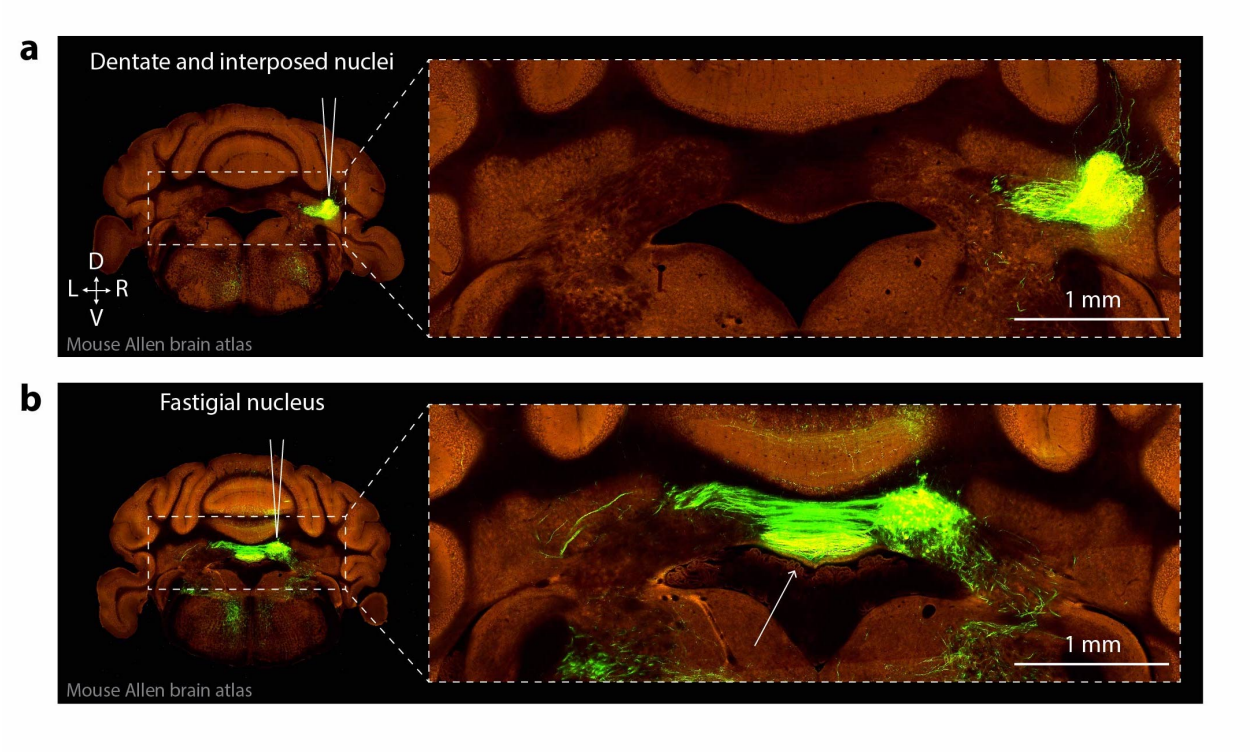

Supplementary Figure 12. Cerebellar stereotactic AAV injection site reveals successful targeting of deep cerebellar nuclei. (a) Coronal section after a unilateral cerebellar injection with dentate and interposed nuclear expression. Axons are visible exiting from nuclei. (b) Coronal section after a unilateral cerebellar injection (different animal) demonstrating fastigial nuclear expression. Axons can be visualized exiting bilaterally from the cerebellum.

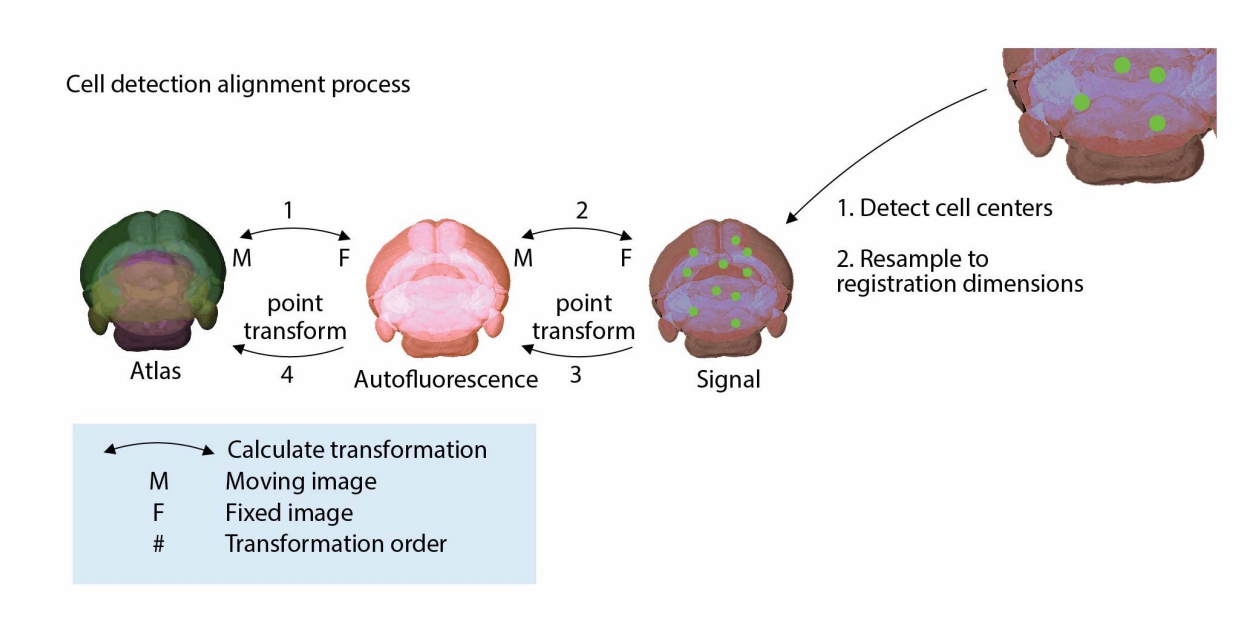

Supplementary Figure 13. Cell center anatomical assignments require multiple transformations. Cell center anatomical assignment requires learning mapping between atlas and signal space. The optimal approach is determining the transformations of atlas (moving) to autofluorescence (fixed) and autofluorescence to signal space. Detected cell centers that have been resampled to registration volume dimensions can be point transformed and anatomically assigned.

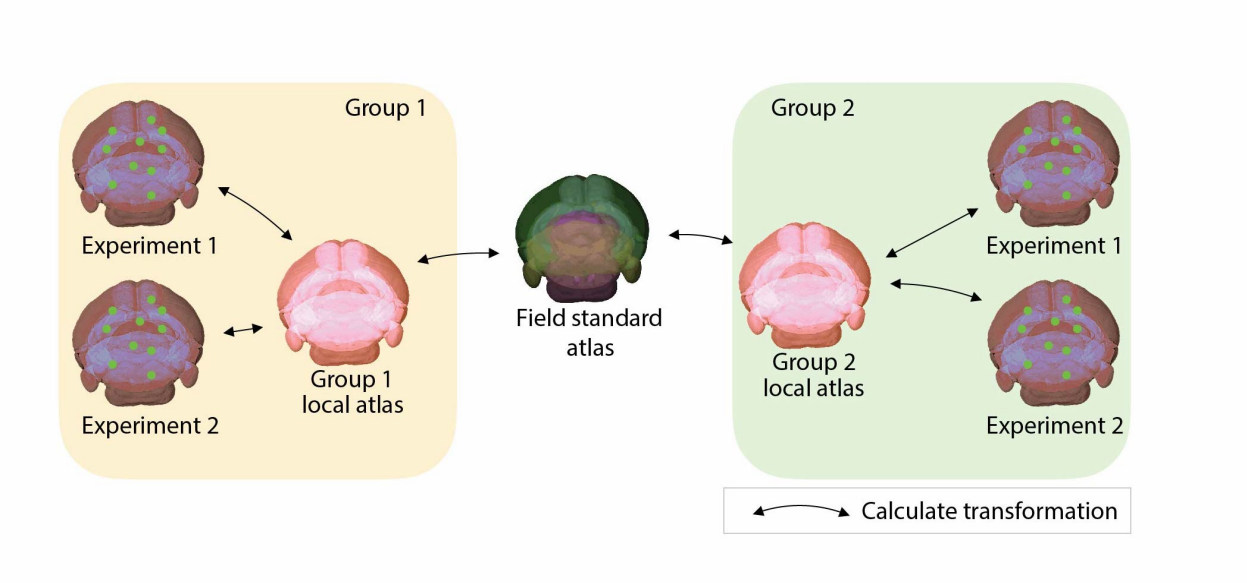

Supplementary Figure 14. A template solution for anatomical commutability between groups. Schematic depicting a solution of balancing considerations for project specific atlas requirements while maintaining consistency with field standards. Groups independently generate local atlases with all features required in their respective projections. Each experiment can accurately be registered with the local atlas. Each group then determines transformation between their local atlas and the field standard, allowing for anatomical commutability across groups. Line with arrows represents determining a transformation between two volumes.

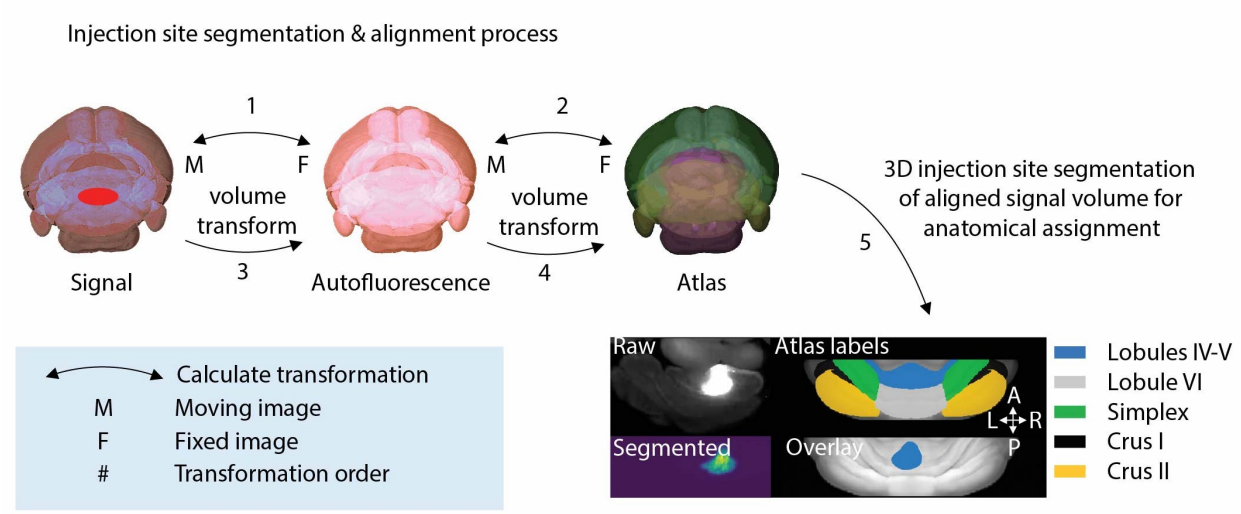

Supplementary Figure 15. Injection site segmentation and alignment process. Injection site anatomical assignment is most efficiently done by mapping signal space (moving) with atlas space (fixed). After the signal image transformation into atlas space, the injection site can be easily segmented and voxels anatomically assigned. F, fixed image; M, moving image. The lower half of B shows an example of segmenting a raw injection site and anatomically assigning to vermal cerebellar lobules IV/V and VI.

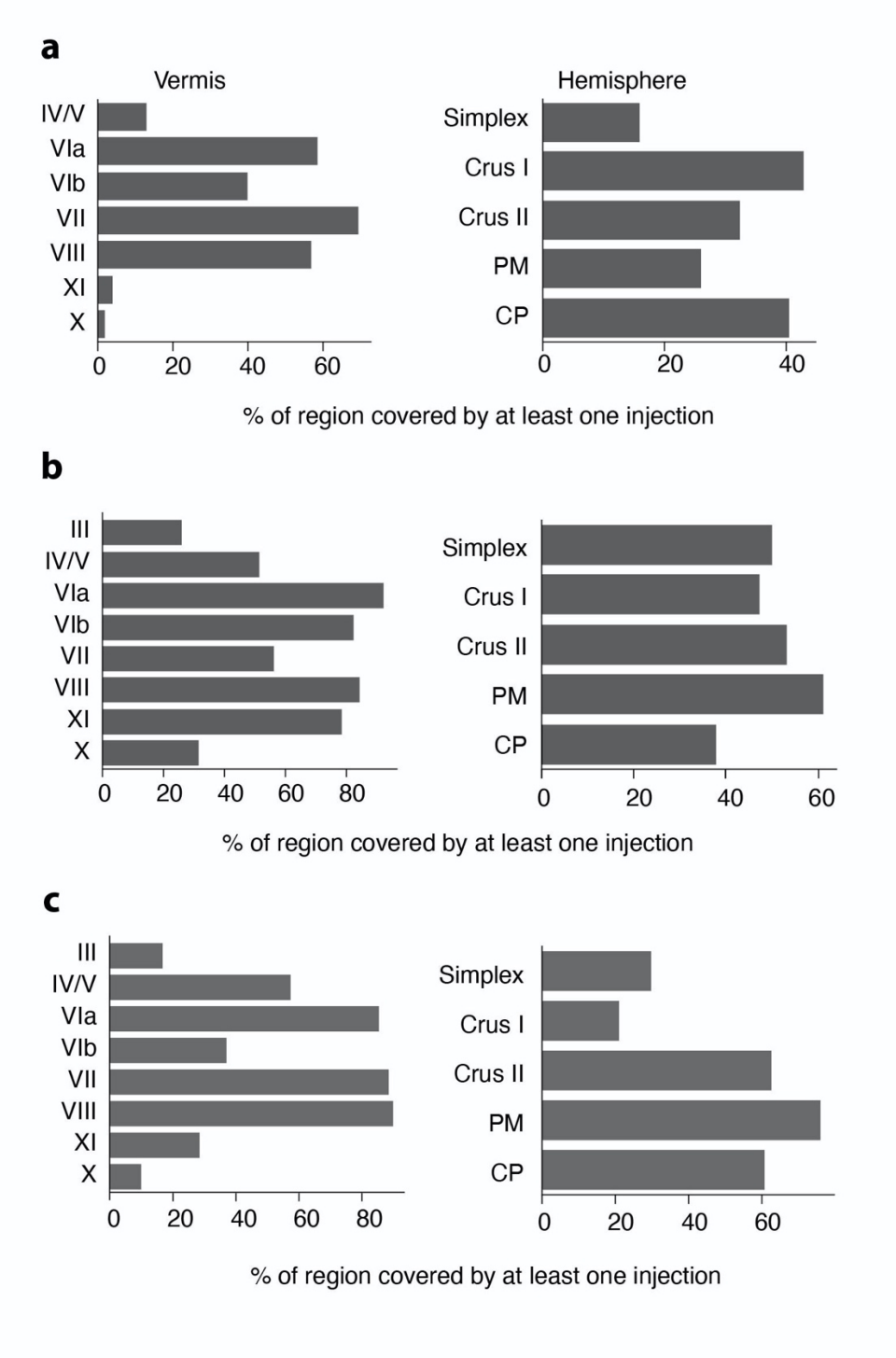

Supplementary Figure 16. Graphs show percent of cerebellar cortical region covered by at least 1 injection after automated injection site quantification of H129-VC22 and PRV injected brains. Brains used in the H129 thalamic cohort (n=23) (a), the H129 neocortical cohort (n=33) (b), and the PRV neocortical cohort (n=25) (c).